The Thesis Committee for Jérôme Sicard
Certifies that this is the approved version of the following thesis:

Investigation of an Extremely Flexible Stowable Rotor for Micro-helicopters

APPROVED BY
SUPERVISING COMMITTEE:

Supervisor: ______________________________
Jayant Sirohi

____
Jeffrey K. Bennighof

Investigation of an Extremely Flexible Stowable Rotor for Micro-helicopters

by

Jérôme Sicard, B.S.

THESIS

Presented to the Faculty of the Graduate School of

The University of Texas at Austin

in Partial Fulfillment

of the Requirements

for the Degree of

MASTER OF SCIENCE IN ENGINEERING

The University of Texas at Austin

May 2011

Dedicated to my brother Frédéric.

Abstract

Investigation of an Extremely Flexible Stowable Rotor for Micro-helicopters

Jérôme Sicard, M.S.E.
The University of Texas at Austin, 2011

Supervisor: Jayant Sirohi

This thesis describes the analysis, fabrication and testing of a rotor with extremely flexible blades, focusing on application to a micro-helicopter. The flexibility of the rotor blades is such that they can be rolled into a compact volume and stowed inside the rotor hub. Stiffening and stabilization of the rotor is enabled by centrifugal forces acting on a tip mass. Centrifugal effects such as bifilar and propeller moments are investigated and the torsional equation of motion for a blade with low torsional stiffness is derived. Criteria for the design of the tip mass are also derived and it is chosen that the center of gravity of each blade section must be located ahead of the aerodynamic center.

This thesis presents the design of 18-inch diameter two-bladed rotors having untwisted circular arc airfoil profile with constant chord. A systematic experimental investigation of the effect of various blade parameters on the stability of the rotor is conducted in hover and forward flight. These parameters include blade flexibility

in bending and torsion, blade planform and mass distribution. Accordingly, several sets of blades varying these parameters are constructed and tested. It is observed that rotational speed and collective pitch angles have a significant effect on rotor stability. In addition, forward flight velocity is found to increase the blade stability.

Next, the performance of flexible rotors is measured. In particular, they are compared to the performance of a rotor with rigid blades having an identical planform and airfoil section. It is found that the flexible blades are highly twisted during operation, resulting in a decreased efficiency compared to the rigid rotor blades. This induced twist is attributed to an unfavorable combination of tip body design and the propeller moment acting on it. Consequently, the blade design is modified and three different approaches to passively tailor the spanwise twist distribution for improved efficiency are investigated. In a first approach, extension-torsion composite material coupling is analyzed and it is shown that the centrifugal force acting on the tip mass is not large enough to balance the nose-down twist due to the propeller moment. The second concept makes use of the propeller moment acting on the tip mass located at an index angle to produce an untwisted blade in hover. It is constructed and tested. The result is an untwisted 18-inch diameter rotor whose maximum Figure of Merit is equal to 0.51 at a blade loading of 0.14. Moreover, this rotor is found to be stable for any collective pitch angle greater than 11 degrees. Finally, in a third approach, addition of a trailing-edge flap at the tip of the flexible rotor blade is investigated. This design is found to have a lower maximum Figure of Merit than that of an identical flexible rotor without a flap. However, addition of this control surface resulted in a stable rotor for any value of collective pitch

angle. Future plans for increasing the efficiency of the flexible rotor blades and for developing an analytical model are described.

Table of Contents

List of Tables

List of Figures

Chapter 1

Introduction

The beginning of the 21^{st} century has seen the emergence of a new class of vehicles called Micro Aerial Vehicles (MAVs). MAVs, as originally defined by DARPA [5], include any Unmanned Air Vehicle (UAV) whose length dimensions are less than 6 in. (15.2 cm) and whose gross takeoff weight is approximately 7 oz. (200 gm) or less. The development of MAVs was initiated in order to meet new military needs; potential missions include military intelligence, surveillance, and reconnaissance (ISR) missions. Their conception was spurred by recent advances in system miniaturization. The low cost associated with flight and manufacturing, relative simplicity, adaptability, and minimal need for support encourages continual development of their mission capability. A wide range of latent commercial applications also exist [6], which includes police surveillance, damage assessment and fire and rescue operations. Because of their size, MAVs are ideally suited to operate in indoor environments such as in buildings or caves.

Among the types of MAVs in development, rotary-wing MAVs play an important role. Similar to their full-scale counterparts, micro-helicopters hover efficiently and possess precise landing capabilities, which suit them for surveillance missions in confined spaces [7, 8]. However, there are several challenges inherent to their design that should be addressed before fully taking advantage of their benefits. The complications mainly relate to obstacle detection and avoidance, decrease of gust sensitivity during outdoor flight, and increase of mission endurance. To fully exploit the favorable characteristics and address the challenges associated with the survivability and durability of these vehicles, it becomes necessary to investigate disparate blade materials and configurations.

One of the anticipated applications of micro-helicopters is to navigate through complex, clustered areas. In such environments, there is a high likelihood of blade collision with obstacles. In this event, a rotary-wing MAV with conventional rigid rotor blades would sustain permanent blade damage and may crash upon impact. Additionally, obstacle avoidance by means of maneuverability as well as the ability to access confined spaces are severely hampered by the constraint of a fixed rotor diameter. These concerns could be addressed by employing flexible, stowable rotor blades in the design of micro-helicopters. Upon collision, flexible blades increase the probability of vehicle survival and recovery, because they can spring back to their natural position and are less likely to be permanently damaged. Flexible rotor blades can also provide the ability to modify the rotor diameter in-flight. Because of the negligible stiffness of its structure, the rotor blade can be rolled up into a cylindrical shape and be retracted into the rotor hub (Figure 1.1(a) and Figure 1.1(b)). As a result, the micro-helicopter can morph its rotor to a range of diameters between a high and a low limit based on mission requirements. Another disadvantage of micro-helicopters is their sensitivity to gusts which limits their outdoor flight capability. Reducing the rotor diameter during outdoor cruise flight can decrease gust

(a) Blades extended (b) Blades retracted

Figure 1.1: Stowable flexible rotor concept

sensitivity by increasing its disk loading.

There have been several research efforts in the past focused on flexible rotor blades to improve the high speed performance of full-scale helicopters. However, a systematic investigation of the feasibility of flexible rotor blades for micro-helicopters has not been reported in the literature to date.

Chapter 2

State of the Art

The flexible, stowable rotor concept emerged in the 1960's as a means to achieve two goals. Firstly, a major technical challenge was to attain high cruise velocities. As a matter of fact, high advancing blade tip Mach numbers prevent full-scale helicopters from achieving cruise speeds equivalent to fixed wing aircrafts (maximum speed around 180 knots). Variable rotor diameter, and even stowable rotor concepts were proposed to address this issue. One such example is the variable-diameter rotor for the Sikorsky Telescoping Rotor AirCraft (TRAC). [9] The rotor blades were designed to change their length in flight by means of a differential gear arrangement in the rotor hub that was coupled to the main rotor shaft in rotation. Laboratory and wind-tunnel tests were successfully performed on a 9-ft diameter model scale rotor. Airspeeds of up to 400 knots were attained with the rotor in the minimum diameter configuration. The major advantage of the variable-diameter rotor was that the rotational speed remained constant, while the major disadvantage was the additional mechanical complexity and weight added to the rotor system.

A second goal was to develop structurally light helicopters capable of lifting heavy loads. Expandable flexible blades were attractive as they propose a lightweight solution to decrease the disk loading by increasing the rotor diameter (the disk loading is the ratio of the helicopter weight to the total main rotor disc area). At NASA Langley, Winston [1, 2] studied the behavior of a 30-ft diameter, extremely flexible rotor. The rotor blades were constructed of a thin non-porous fabric airfoil surface attached to two steel rods to form the leading and trailing edges as shown in Figure 2.1. A tip mass with an aerodynamic stabilizer was secured to the end of the blade. It provided resistance to bending and torsion by means of centrifugal forces. The chordwise location of the center of gravity of the tip mass was set at the blade quarter chord. This was consistent with the results of a classical 2D section approach to determine the aeroelastic stability of a rotor blade. An elementary aeroelastic analysis also revealed that blade stability was independent of the rotational speed. Additionally, Winston performed hover experiments in order to compare the performance and efficiency of flexible rotors to conventional rigid rotors. In these experiments, stability was assessed using vibration data. Figures of Merit (FM) were computed to evaluate the efficiency. This non-dimensional coefficient is a measure or the rotor efficiency and is defined as the ratio of the minimum possible power required to hover to the actual power required to hover. [10] Although high levels of vibration indicated that portions of the blades were stalled at high root pitch angles, the thrust coefficient continually increased in the range of root pitch angles tested. Because of the nature of the blades, the high twist along the blade was such that the outboard sections of the blade remained unstalled. The Figure of Merit of the flexible rotor was relatively low ($FM_{max} = 0.43$ for a rotor mean lift coefficient of 1.1), which was attributed to blade deformation. The poor airfoil section (which resulted from the blunt leading and trailing edges formed by

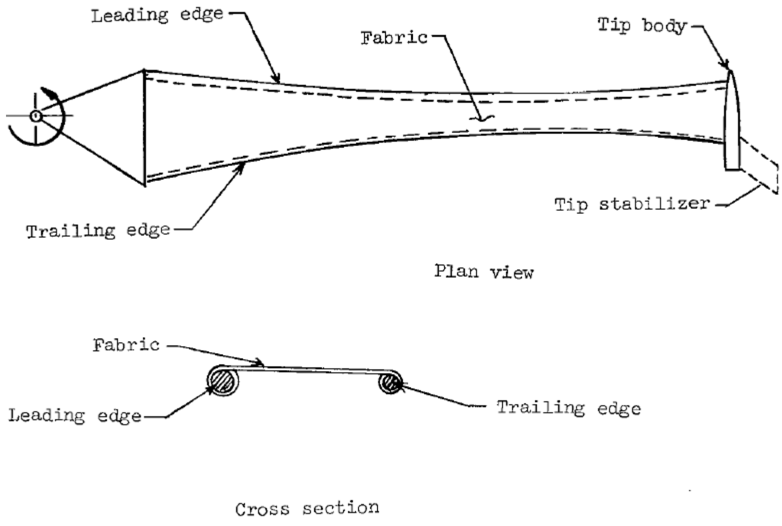

Figure 2.1: NASA rotor blade, from Reference [1, 2]

the structural rods) also contributed to the low efficiency. In addition, tip speed was found to be a very important parameter as it affected the camber not only by centrifugal stiffening, but also through aerodynamic forces. From his analysis, Winston concluded that flexible rotor efficiency could be enhanced by controlling the pitch and stabilizer incidence and by incorporating a more aerodynamic planform in his design.

Another study was conducted by Pruyn and Swales [3] in the early 1960's. They described the development and testing of a flexible rotor blade at Kellett Aircraft Corporation. The blade consisted of a fabric or stainless steel membrane between two cables that formed the leading and trailing edges (Figure 2.2). A tip mass provided the centrifugal stiffening and the blade could be rolled up into a cylinder. It was shown analytically that the flexible blade weighed only 62.5% of the weight of a conventional blade for the same coning angle. In addition, the dynamic stability

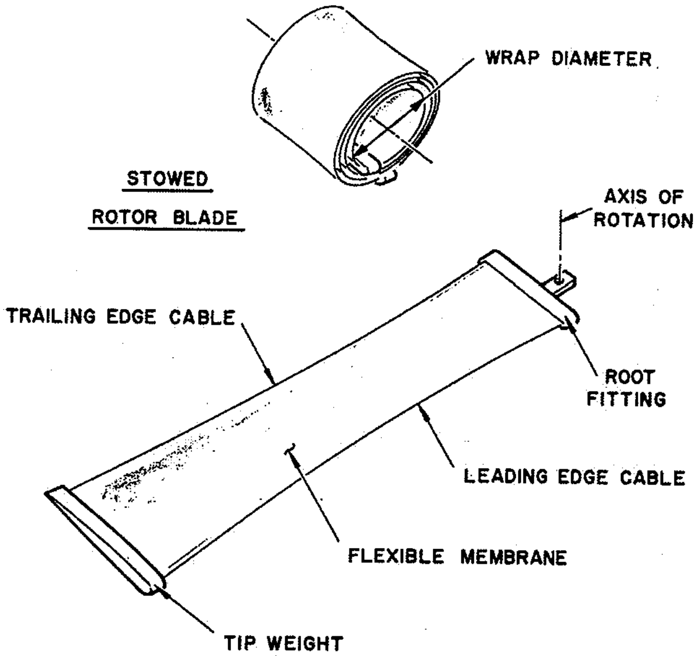

Figure 2.2: Kellett rotor blade, from Reference [3]

of the blades was analyzed and was found to be independent of the rotational speed. A ducted two-bladed flexible rotor of diameter 2.9 ft and an unducted two-bladed flexible rotor of diameter 4 ft were tested in hover and in axial autorotation in a wind tunnel. The flexible rotors were able to sustain a disk loading of up to 100 psf, however, whirl test data showed poor rotor performance, which was attributed to the high drag of the tip weight as well as leading and trailing edge cables. The study concluded that flexible rotors of this design were feasible and that more analysis was required to establish the stability limits of the rotor.

Sikorsky Aircraft Corporation studied an extremely flexible rotor blade that consisted of a thin metal ribbon with a tip mass, in the purpose of designing a high-speed full-scale compound helicopter. [11]. This rotor blade could be rolled up into a cylinder and enclosed within the rotor hub. Although promising, the concept was not pursued beyond the model stage in favor of other, lower risk approaches to achieving high speed.

At the Martin Company, Goldman [12] described the development and hover testing of an extremely flexible rotor. The rotor blades consisted of segmented balsa ribs with a flexible skin, supported by 1/16 inch diameter cables at the leading edge and trailing edge. The cables were attached to a tip pod with an electrically driven propeller that provided the torque required by the rotor. In the cases where flutter occurred, a torsional deflection similar to the first mode of a fixed-fixed shaft was observed in high-speed videos. An analysis of the blade including torsion and flapping degrees of freedom was performed using an influence coefficient approach. For a stable blade, it was determined that the blade center of gravity must be ahead of the elastic axis, and the elastic axis must be ahead of the aerodynamic center. It was concluded that it is feasible to design highly flexible, low-disk loading rotors offering significant performance benefits.

Finally, Roeseler [13] described the analysis and hover testing of a 3 ft radius, two-bladed ribbon rotor. The blade consisted of a 0.005 inch thick mylar sheet with a tip mass. Theoretical stability boundaries were calculated assuming rigid flapping and linear twisting modes. A position of the tip mass was determined to ensure stability and prevent luffing of the trailing edge. The mylar blade was found to be susceptible to fatigue failure. Stable operation could not be achieved without enclosing the tip mass in an aerodynamic fairing. The same criteria for stability as those discussed by Goldman [12] were determined from the analysis.

From the studies described previously, it can be seen that the concept of an extremely flexible rotor that can be rolled up into a compact volume appears feasible. Efficiency of such rotor blades was found to be poor because of low chordwise stiffness of the blades, poor airfoil performance and high drag of the tip mass. The limits of stability in hover and forward flight were not fully explored, and no further studies have been reported in the literature on this type of rotor beyond the late 1960's. While the concept appears promising, limited data exists on their behavior, especially at the micro-helicopter scale. It is possible that the performance of these rotors can be enhanced as a result of technological advancements in materials as well as careful design. Key technical challenges as well as possible solutions need to be identified.

Chapter 3

Present Approach

3.1 Proposed flexible rotor blade concept

The flexible rotor design explored in the present approach consists of a thin carbon-fiber composite sheet in conjunction with a tip body. This tip body is inherent to the development of any flexible blade as it is necessary to provide centrifugal stiffening and stabilize the rotor in flight. Its mass is of the same order of magnitude as the blade mass. This allows to adjust the chordwise location of the overall center of gravity. This position is chosen based on a 2D typical section aeroelastic analysis. A two-bladed flexible rotor system is shown in the deployed state in Figure 3.1. The composite sheet is designed to sustain the centrifugal loads on the blade, eliminating the need for cables at the leading and trailing edges. The blade cross-section is chosen to be a circular arc because it is efficient at the low Reynolds numbers at which micro-helicopters operate [7, 8, 14] ($Re \sim 5 \times 10^4$).

3.2 Phase 1: Preliminary investigations on the stability and performance of flexible rotor blades

In a first phase, the influence of various parameters on the stability and performance of flexible rotor blades was investigated. The role of bending and tor-

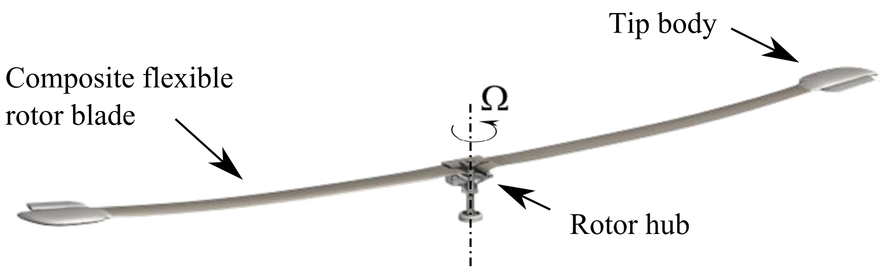

Figure 3.1: Schematic of proposed flexible rotor blade

sional stiffness was explored by fabricating several sets of blades using different combinations of composite fibers and resins. A detailed exploration of the dependence of control parameters such as collective pitch angle, speed of rotation and mass balance on the stability of the blades was conducted. Additionally, attempts to reduce the drag of the tip mass were made. Flexible blade designs with a fairing around the tip body were constructed and tested. The goal of the first phase was to collect sets of experimental data in hover and in forward flight in order to create baselines to be used in comparison with future improved designs.

3.3 Phase 2: Twist control of an extremely flexible rotor

In a second phase, the control of twist deformations was considered. It was observed in the past studies [1] that, due to the extremely low torsional stiffness of the flexible rotors, pitch angle inputs at the root could not be transferred to the tip of the blade. At the same time, it was noticed that centrifugal forces tend to align the tip body such that its axis of minimum inertia is parallel to the rotor plane, resulting in a highly twisted rotor blade with a poor Figure of Merit. This restoring moment is called propeller moment (or dumbbell effect). It is highly significant for flexible blades with negligible torsional stiffness. Three different approaches to modify the twist distribution along the span were investigated.

In a first approach (Concept A), the properties of coupling allowed by composite materials were inspected in order to offset the negative twist distribution produced by the propeller moment. In particular, a composite laminate with extension-torsion coupling was analyzed to make use of the centrifugal force in order to modify the twist distribution along the span of the flexible blade.

The second approach (Concept B) made use of the propeller moment by introducing an index angle between the chord of the blade and the principal axis of the tip body.

The third approach (Concept C) involved the use of trailing-edge flaps [15] in order to produce pitching moment changes. The trailing-edge flap could not only provide primary control inputs to the rotor system, but also acted as a tip body in order to stiffen the blade by means of centrifugal force.

While the proposed concept of an extremely flexible rotor envisions the use of micro-actuators to actively control the pitch angle of the blades at a desired value, this work focuses only on passively induced twist. Similarly, the tip body will contain in the future a miniature inertial measurement unit (IMU) with which the position of the blade tip can be measured at any instant of time. This IMU will provide the sensory feedback for the stabilization and control of the flexible rotor system.

Chapter 4

Analysis of a flexible rotor

4.1 Dynamics and stability analysis

4.1.1 Effect of the centrifugal force on a rotating blade

The behavior of a rotor blade with extremely low structural stiffness is dominated by centrifugal forces. For example, in a purely articulated rotor , which has zero non-rotating stiffness in rigid flap, centrifugal forces result in a fundamental flap frequency slightly greater than one per revolution (1/rev). In a similar way, for a rotor blade with negligible torsional stiffness, the fundamental torsional frequency is slightly greater than 1/rev. The objective of this analysis is to see how centrifugal stiffening changes the rotating natural frequencies of an extremely flexible rotor.

Centrifugal forces stiffen the blade in the torsional degree of freedom in two ways: the dumbbell effect and the bifilar effect. The dumbbell effect (or tennis racket effect) is also known as the propeller moment, and arises due to the tendency of the centrifugal forces to rotate the rotor blade to flat pitch. The bifilar moment, also known as the trapeze moment, arises from the twisting of the fibers causing an effective shortening of the rotor blade. In conventional rotor blades, the propeller moment is more important. However, in the present case, the bifilar moment can be significant due to the high torsional flexibility of the rotor blade. Both bifilar and propeller moments must be studied.

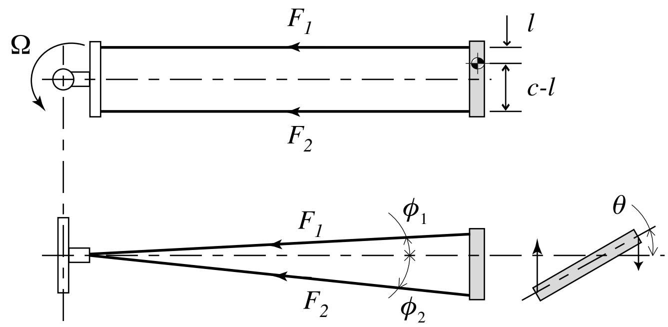

Figure 4.1: Schematic of bifilar moment in a flexible rotor composed of two cables

4.1.1.1 Torsional stiffness and rotating natural frequency due to bifilar moment

We consider the case of a flexible rotor blade of constant chord, consisting of a tip mass supported by two cables, forming the leading and trailing edges of the blade. The plan view of such a blade is shown in Figure 4.1. Solving for the tensile forces in each of the cables, we get

$$F_1 = \left(1 - \frac{l}{c}\right) m_T \, \Omega^2 \, R \tag{4.1}$$

$$F_2 = \frac{l}{c} m_T \, \Omega^2 \, R \tag{4.2}$$

where l is the position of the center of gravity of the tip mass, c is the blade chord, m_T is the tip mass, R is the blade radius and Ω is the rotational speed. It can be deduced from the above derivation that the effective elastic axis of the blade is defined by the chordwise position of the center of gravity of the tip mass. In the general case, it can be shown that the elastic axis of the rotor blade is defined by the chordwise position of the centroid of the radial stress field along the blade span [12, 13]. Accordingly, for small torsional deflections, the torsional moment on the rotor blade due to the bifilar effect is given by

$$M_\theta = F_1 \sin\phi_1 l \cos\theta + F_2 \sin\phi_2 (c - l)\cos\theta \tag{4.3}$$

$$\simeq F_1 \sin\phi_1 l + F_2 \sin\phi_2 (c - l) \tag{4.4}$$

where ϕ_1 and ϕ_2 are the angles between the tangent to the cables at the point of attachment to the tip mass and the horizontal plane. Assuming a linear torsional deflection mode shape, the deflected cables will be straight lines, and the relevant angles are given by

$$\sin\phi_1 = l \sin\theta / R \tag{4.5}$$

$$\sin\phi_2 = (c - l)\sin\theta / R \tag{4.6}$$

Expressing the bifilar restoring moment in terms of an equivalent torsional stiffness, and substituting for the angles from above,

$$M_\theta = K_\theta \theta \tag{4.7}$$

$$= l(c - l) m_T \Omega^2 \theta \tag{4.8}$$

From the above equation, the torsional stiffness due to the bifilar effect is obtained as

$$K_\theta = l(c - l) m_T \Omega^2 \tag{4.9}$$

and the rotating natural frequency corresponding to the linear deflection mode is

$$\frac{\omega_\theta}{\Omega} = \sqrt{\frac{m_T c^2}{I_T}\left(\frac{l}{c} - \frac{l^2}{c^2}\right)} \tag{4.10}$$

where I_T is the torsional moment of inertia of the tip mass about its center of gravity. The variation of the rotating torsional natural frequency ($\frac{\omega_\theta}{\Omega}$) with chordwise

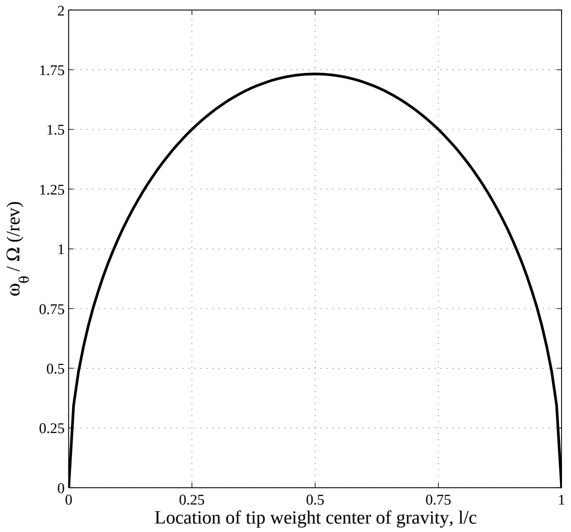

Figure 4.2: Influence of tip weight balance on torsional frequency

position of the tip mass center of gravity is plotted in Figure 4.2. Note that for a cylindrical tip mass of uniform density ($I_T = m_T c^2/12$), the maximum torsional frequency occurs when the tip mass is centered between the two cables ($l/c = 0.5$). In this condition, the torsional frequency becomes $\omega_\theta/\Omega = \sqrt{3} = 1.732$/rev.

4.1.1.2 Torsional stiffness and rotating natural frequency due to propeller moment

The torsional stiffness due to the propeller moment is now derived. We consider an infinitesimal element of the blade shown on Figure 4.3. The centrifugal force on this element of mass *dm* is

$$F_{CF} = dm\,\Omega^2\,\sqrt{x^2 + y^2} \tag{4.11}$$

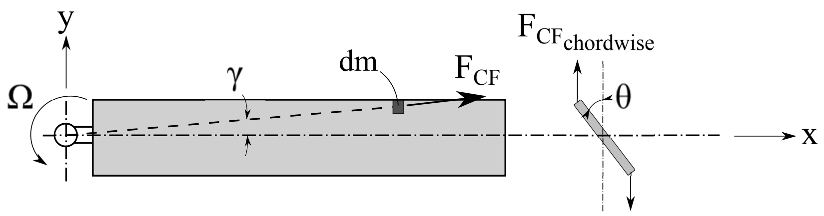

Figure 4.3: Schematic of propeller moment acting on a rotating blade

The chordwise component of the centrifugal force is

$$F_{CF}^{chord} = F_{CF}\,\sin\gamma \tag{4.12}$$

$$= F_{CF}\,\frac{y}{R} \tag{4.13}$$

$$= dm\,\Omega^2\,\sqrt{x^2+y^2}\,\frac{y}{\sqrt{x^2+y^2}} \tag{4.14}$$

$$= dm\,\Omega^2\,y \tag{4.15}$$

Thus, the moment about the *y-axis* associated with F_{CF} (for a small angle θ) is

$$dM_\theta = F_{CF}^{chord}\,y\,\sin\theta \tag{4.16}$$

$$\simeq F_{CF}^{chord}\,y\,\theta \tag{4.17}$$

$$= dm\,\Omega^2\,y^2\,\theta \tag{4.18}$$

And the propeller moment acting on the entire blade is

$$M_\theta^{CF} = \int_{span}\int_{chord} dM_\theta \tag{4.19}$$

$$= \Omega^2\,\theta\int_{span}\int_{chord} y^2 dm \tag{4.20}$$

$$= I_\theta\,\Omega^2\,\theta \tag{4.21}$$

From the above equation, the torsional stiffness due to the propeller effect is obtained as

$$K_\theta = I_\theta \, \Omega^2 \tag{4.22}$$

and the corresponding rotating natural frequency is

$$\frac{\omega_\theta}{\Omega} = 1 \tag{4.23}$$

4.1.1.3 Equation of torsional motion of the blade

Combining the effects of the bifilar and the propeller moments previously presented, the equation of torsional motion of a flexible blade with tip mass can be derived. Its solution will yield the torsional frequencies of the system.

While no detailed and specific aeroelastic analysis of a flexible rotor has been reported in the literature, simple studies such as the one described by Winston [1] were performed considering a 2-D airfoil section undergoing vertical translational and pitching motion. Following the derivation for rigid blades (shown in Section 4.1.2), he identified the flutter and divergence boundaries for a rotor blade of low mass per unit length, infinite flexibility in bending and torsion, and with cables as the main structural members. Under these assumptions, he found that in order to achieve stable operation for any value of tip mass, the elastic axis should be ahead of the aerodynamic center , and the blade section center of gravity should be ahead of the elastic axis. However, we will see that the case presented in this thesis does not fall under the previous assumptions. The mass of the blade membrane is of the same order as the tip mass and cannot be neglected. Moreover, bending and torsional stiffnesses are small but not zero. Nevertheless, in order to compare the results with past experiments, each design presented in this thesis will ensure that the blade section center of gravity is located ahead the aerodynamic center (approximated to be at the quarter-chord point for thin cambered profiles [16]).

4.1.2 Dynamics stability

The next sections show derivations of stability criteria for the pitch-flap coupled motion of rigid rotor blades. The following assumptions are made:

1. rigid articulated blade with flap (bending) and pitch (torsion) degrees of freedom
2. 2-D airfoil section
3. coincident flapping and pitching hinge, offset e from the rotor axis of rotation

4.1.2.1 Coupled pitch-flap equations of motion

The equation for flapping motion is derived from equilibrium of moments about the flap hinge. The forces causing these moments on a blade section (Figure 4.4(a) and 4.4(b)) are:

- Aerodynamic force dF_z, with moment arm $(y-e)$
- Centrifugal force $dm\,\Omega^2[e+(y-e)\cos\beta] \simeq dm\,\Omega^2 y$, with moment arm $(y-e)\sin\beta - x_I \sin\theta \simeq (y-e)\beta - x_I\theta$, where x_I is the distance between the blade section center of gravity and the feathering (or pitching) axis

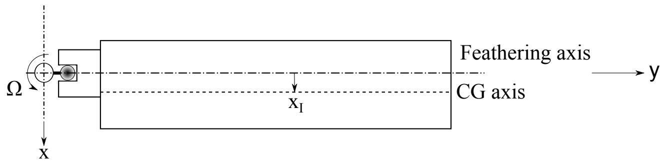

(a) Top view

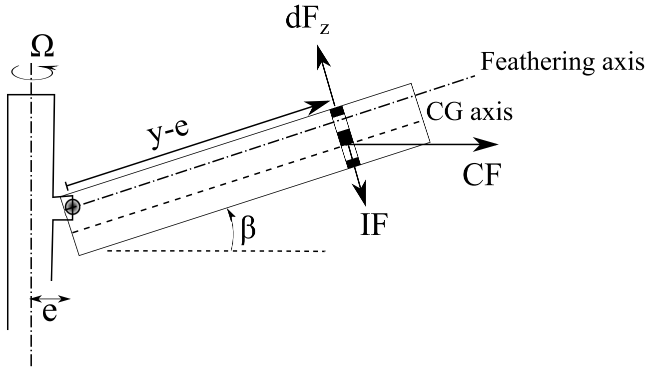

(b) Side view

Figure 4.4: Blade section flapping moments

- Inertial force $dm\,\ddot{\beta}(y-e) - dm\,\ddot{\theta}x_I$, with moment arm $(y-e)$

Moment equilibrium at the hinge implies

$$\int_e^R dm\,\ddot{\beta}(y-e)^2 - \int_e^R dm\,\ddot{\theta}x_I(y-e) + \int_e^R dm\,\Omega^2 y[(y-e)\beta - x_I\theta] = \int_e^R dF_z(y-e) \tag{4.24}$$

where β is the flapping angle and θ is the pitching angle. Using the moments of inertia defined in Appendix 1 and defining $M_\beta = \int_e^R dF_z\,(y - e)$, we obtain

$$I_\beta\ddot{\beta} - I_x\ddot{\theta} + S_\beta\Omega^2\beta - I_x\Omega^2\theta + \int_e^R dm\,\ddot{\theta}x_I e = M_\beta \tag{4.25}$$

The last term of the left-hand side is negligible as x_I and e are small. Furthermore, time derivatives are replaced by azimuthal derivatives thanks to the following transformation (Ψ is the azimuthal angle)

$$\dot{\beta} = \frac{d\beta}{d\Psi}\frac{d\Psi}{dt} = \Omega \overset{*}{\beta} \tag{4.26}$$

$$\ddot{\beta} = \Omega^2 \overset{**}{\beta} \tag{4.27}$$

Finally, the flap equation of motion is

$$\overset{**}{\beta} + \nu_\beta^2 \beta - I_x^* (\overset{**}{\theta} + \theta) = \gamma \overline{M}_\beta \tag{4.28}$$

where $\gamma = \frac{\rho c C l_\alpha R^4}{I_\beta}$ is the Lock number and $\overline{M_\beta} = \frac{M_\beta}{\rho c C l_\alpha \Omega^2 R^4}$ is dimensionless.

The pitch equation of motion is obtained from equilibrium of moments about the feathering (or pitching) axis. The moments acting on a blade section (Figure. 4.5) are

- Nose-up aerodynamic moment M_θ about the feathering axis

- Nose-down propeller moment $dI_\theta\, \Omega^2 \theta$ about the feathering axis, and centrifugal force $dm\, \Omega^2 y \sin\beta \cos\theta \simeq dm\, \Omega^2 y \beta$ acting at the center of gravity with moment arm x_I about the feathering axis

- Inertial moment $I_O \ddot{\theta}$ about the section center of gravity, inertial force due to flapping motion $dm\, (y - e)\ddot{\beta}$ acting on the center of gravity with moment arm x_I, and the inertial force due to pitching motion around the feathering axis $dm\, \ddot{\theta} x_I$ acting on the center of gravity with moment arm x_I

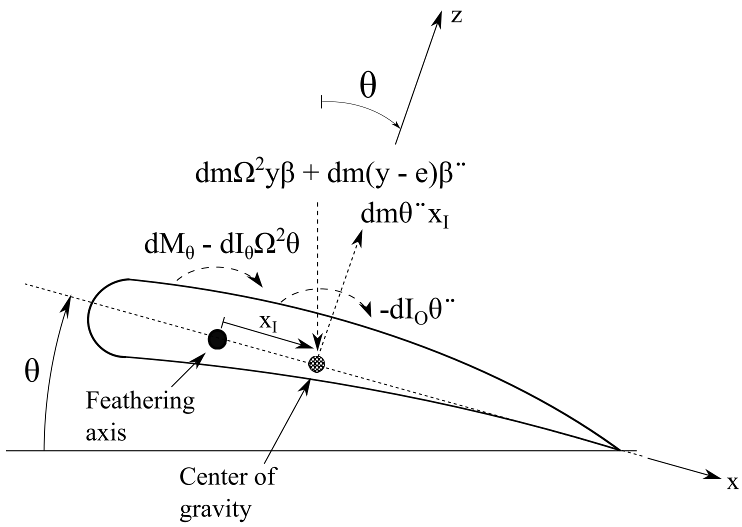

Figure 4.5: Blade section pitching moments

Moment equilibrium at the feathering axis gives

$$-\int_e^R dm\,\ddot{\theta}x_I^2 - \int_e^R dI_O\ddot{\theta} + \int_e^R dm(y-e)\ddot{\beta}x_I + \int_e^R dm\Omega^2 y\beta x_I - \int_e^R dI_\theta\Omega^2\theta + \int_e^R dM_\theta = 0 \quad (4.29)$$

I_O is the polar mass moment of inertia of the blade section about the center of gravity. Consequently, from the Huygens-Steiner theorem, $I_\theta = I_O + mx_I^2$ is the section moment of inertia about the feathering axis. Introducing $I_f^* = \frac{I_\theta}{I_\beta}$, and neglecting higher order terms, the pitch equation of motion is

$$I_f^*(\overset{**}{\theta} + \theta) - I_x^*(\overset{**}{\beta} + \beta) = \gamma\overline{M}_\theta \quad (4.30)$$

Combining Equations 4.28 and 4.30, we can write the system of coupled pitch-flap equations of motion

$$\begin{bmatrix} 1 & -I_x^* \\ -I_x^* & I_f^* \end{bmatrix} \begin{Bmatrix} \overset{**}{\beta} \\ \overset{**}{\theta} \end{Bmatrix} + \begin{bmatrix} \nu_\beta^2 & -I_x^* \\ -I_x^* & I_f^* \end{bmatrix} \begin{Bmatrix} \beta \\ \theta \end{Bmatrix} = \gamma \begin{Bmatrix} \overline{M}_\beta \\ \overline{M}_\theta \end{Bmatrix} \quad (4.31)$$

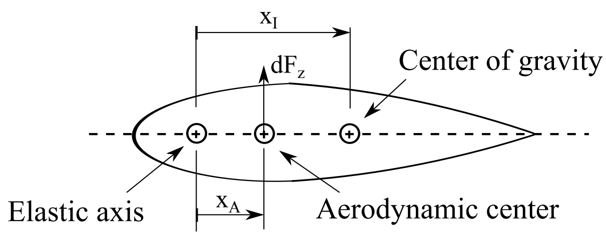

Figure 4.6: Locations of elastic axis, aerodynamic center and center of gravity

The flap and pitch motions are coupled by inertial and centrifugal forces when $I_x^* \neq 0$, that is when the blade center of gravity is offset from the feathering axis ($x_I \neq 0$). Note that in the case of a rigid blade, the elastic axis coincides with the feathering axis.

Assuming hover conditions and a uniform inflow λ_i through the rotor disk, it can be shown that [10]

$$\overline{M}_\beta = \frac{1}{2}\left(\frac{\theta}{4} - \frac{\lambda_i}{3} - \frac{\overset{*}{\beta}}{4}\right) \tag{4.32}$$

$$\overline{M}_\theta = -\frac{1}{2}\frac{x_A}{R}\left(\frac{\theta}{3} - \frac{\lambda_i}{3} - \frac{\overset{*}{\beta}}{3}\right) \tag{4.33}$$

where x_A is the distance from the elastic axis to the aerodynamic center of the blade section (Figure 4.6). Consequently, the coupled differential equations of motion become

$$\begin{bmatrix} 1 & -I_x^* \\ -I_x^* & I_f^* \end{bmatrix}\begin{Bmatrix} \overset{**}{\beta} \\ \overset{**}{\theta} \end{Bmatrix} + \begin{bmatrix} \frac{\gamma}{8} & 0 \\ -\frac{\gamma}{6}\frac{x_A}{R} & 0 \end{bmatrix}\begin{Bmatrix} \overset{*}{\beta} \\ \overset{*}{\theta} \end{Bmatrix} + \begin{bmatrix} \nu_\beta^2 & -I_x^* - \frac{\gamma}{8} \\ -I_x^* & I_f^* + \frac{\gamma}{6}\frac{x_A}{R} \end{bmatrix}\begin{Bmatrix} \beta \\ \theta \end{Bmatrix} = \gamma \begin{Bmatrix} -\frac{\lambda_i}{6} \\ \frac{\lambda_i x_A}{6R} \end{Bmatrix} \tag{4.34}$$

We will now study the stability boundaries of this equation.

4.1.2.2 Pitch-flap divergence

In order to analyze the stability boundaries of the pitch-flap equations of motion, we convert them to perturbation equations and then transform them into the Laplace domain. The result is

$$\begin{bmatrix} s^2 + \frac{\gamma}{8}s + \nu_\beta^2 & -I_x^* s^2 - I_x^* - \frac{\gamma}{8} \\ -I_x^* s^2 - \frac{\gamma}{6}\frac{x_A}{R}s - I_x^* & I_f^* s^2 + I_f^* + \frac{\gamma}{6}\frac{x_A}{R} \end{bmatrix} \left\{ \begin{array}{c} \overline{\beta} \\ \overline{\theta} \end{array} \right\} = \left\{ \begin{array}{c} 0 \\ 0 \end{array} \right\} \tag{4.35}$$

The eigenvalues of this system of equations are the roots of the following characteristic equation

$$\begin{aligned} &\left(s^2 + \frac{\gamma}{8}s + \nu_\beta^2\right)\left(\frac{c^2}{4R^2}s^2 + \frac{c^2}{4R^2} + \frac{\gamma}{6}\frac{x_A}{R}\right) \\ &\qquad - \left(-\frac{3}{2}\frac{x_I}{R}s^2 - \frac{\gamma}{6}\frac{x_A}{R}s - \frac{3}{2}\frac{x_I}{R}\right)\left(-\frac{3}{2}\frac{x_I}{R}s^2 - \frac{3}{2}\frac{x_I}{R} - \frac{\gamma}{8}\right) = 0 \end{aligned} \tag{4.36}$$

where I_x^* and I_f^* have been replaced according to Appendix 1. A divergence instability will occur when a real root goes through the origin of the s-plane into the half plane corresponding to $Re(s) \geq 0$. At the divergence boundary, $s = 0$. Hence, the blade will not experience pitch-flap divergence if

$$\nu_\beta^2\left(\frac{c^2}{4R^2} + \frac{\gamma}{6}\frac{x_A}{R}\right) - \frac{3}{2}\frac{x_I}{R}\left(\frac{3}{2}\frac{x_I}{R} + \frac{\gamma}{8}\right) \geq 0 \tag{4.37}$$

Typically for a rigid blade: $\gamma = 8$, $\nu_\beta = 1.1$, $I_f^* = 0.001$ and $\frac{R}{c} = 10$. Therefore, the previous criterion is (neglecting second-order terms)

$$1.5\,\frac{x_I - x_A}{R} \leq \nu_\beta^2 \frac{c^2}{4R^2} \tag{4.38}$$

It can be seen that if $x_I - x_A < 0$ (center of gravity ahead of the aerodynamic center), then the blade is always free from pitch-flap divergence.

4.1.2.3 Pitch-flap flutter

A flutter instability occurs when a pair of complex conjugate roots crosses the imaginary axis of the s-plane into the right half-plane ($Re(s) \geq 0$). Therefore, we require $s = i\omega$ and the characteristic equation is the following 4th order polynomial in $i\omega$

$$\begin{aligned}\left(1.5\,\frac{x_I}{R} - 0.001\right)(i\omega)^4 + \left(2\,\frac{x_I x_A}{R^2} - 0.001\right)(i\omega)^3 \\ + \left(4.5\,\frac{x_I^2}{R^2} - \frac{1.3x_A - 1.5x_I}{R} - 0.00221\right)(i\omega)^2 \\ + \left(2\,\frac{x_I x_A}{R^2} - 1.3\,\frac{x_A}{R} - 0.001\right)(i\omega) \\ + \left(2.25\,\frac{x_I^2}{R^2} - \frac{1.6x_A - 1.5x_I}{R} - 0.00121\right) = 0 \quad (4.39)\end{aligned}$$

or

$$A(i\omega)^4 + B(i\omega)^3 + C(i\omega)^2 + D(i\omega) + E = 0 \tag{4.40}$$

According to the Routh-Hurwitz stability criterion [17], the blade will be stable if

$$\begin{cases} A, B, C, D, E > 0 \\ BC > AD \\ BCD > AD^2 + B^2E \end{cases} \tag{4.41}$$

The first two conditions are naturally satisfied for typical values of the ratios $\frac{x_I}{R}$ and $\frac{x_A}{R}$. Dropping the second-order terms, the third condition is

$$\frac{x_I - x_A}{R} < \left(\frac{c}{R}\right)^2 \left(\frac{1}{3\sqrt{2}} + \frac{\gamma}{48}\right) \tag{4.42}$$

$$< 0.004 \tag{4.43}$$

Therefore, the condition $x_I - x_A < 0$ ensures again that the blade is pitch-flap flutter free.

4.1.2.4 Luffing

Besides the well known pitch-flap flutter and divergence instabilities, luffing can cause vibration of the membrane of a torsionally extremely flexible rotor blade. The primary reason for this instability is a membrane of an airfoil which cannot carry any compressive loads. The result is characterized by rapid reversals of camber and is considered as a ”low-pitch” phenomenon [1] because it usually can be relieved by increasing the blade-pitch angle. The luffing instability played a major role in the design of fabric-made flexible rotors in the 1960s, as they had almost no stiffness in torsion. However, the matrix composite rotor blades fabricated for this study, although flexible in torsion, have sufficient stiffness to eliminate the luffing instability.

4.2 Design of the tip body

The tip mass is a key feature in the design of a flexible rotor, as it is responsible for stiffening and dynamic stabilization. The first effect is produced by centrifugal forces and depends upon the radial location and the mass of the tip body. While it is optimum to secure it at the tip of the blade, its mass has to be restrained for two reasons. Increasing it results in a decrease of the weight efficiency of the rotor. Secondly, the tip body plays a major role on the mass balance of the blade, and therefore on the stability of the rotor. In particular, it affects the location of the blade center of gravity, which must be located ahead of the aerodynamic center. Therefore, a careful design is required.

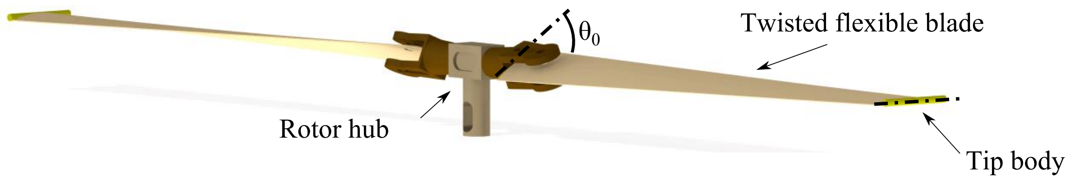

Figure 4.7: Unfavorable twist in the spanwise direction

The design of the tip mass is also influenced by another effect. One of the major conclusions from the first phase of experiments was that the flexible blades were highly twisted during hover operation, especially when tested for large collective pitch angles. This induced twist was unfavorable as it was responsible for a large increase in profile power, hence, a loss in efficiency. Its cause came from the propeller moment presented in Section 4.1.1.2 acting on the rotating tip body and tending to drive the blade tip to flat pitch (see Figure 4.7). We are interested in ways to passively tailor the blade twist distribution. Accordingly, the following section analyzes three solutions to passively alleviate the unfavorable twist distribution generated by the propeller moment.

4.3 Passive control of the twist curvature

4.3.1 Concept A: Twist control by means of composite material coupling

The objective is to develop a flexible rotor blade with a composite laminate designed such that the unfavorable twist distribution vanishes during operation in hover. A flexible blade with no means to control the twist distribution constitutes the baseline. First, the collective pitch angle yielding to the maximum Figure of Merit of this baseline design must be identified. This angle is denoted θ_{index}. When

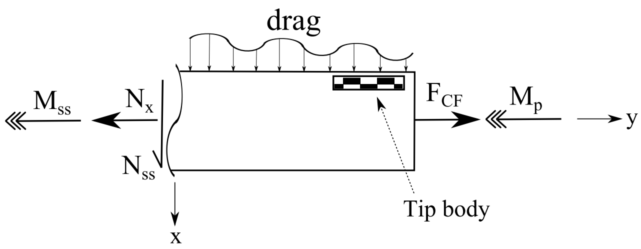

Figure 4.8: Free body diagram of the rotating blade

spinning in this condition, the tip of the flexible blade B1 rotates at flat pitch. In order to minimize the unfavorable twist, the goal of the composite coupling is to produce a nose-up moment that results in a twist angle at the tip of θ_{index} degrees. The proposed concept is to use extension-torsion composite coupling. The centrifugal force acting on the tip mass in conjunction with an appropriate composite lay-up will generate the desired twist deformations.

Figure 4.8 is a free body diagram showing forces and moments applied on the tip of the flexible blade in rotation. The equations of equilibrium are

$$N_x = F_{CF} \tag{4.44}$$

$$M_{ss} = -M_p \tag{4.45}$$

At any spanwise location, the total centrifugal force and total propeller moment (nose down) are given by

$$F_{CF} = \int_y^R \Omega^2 m_y y dy + m_T \Omega^2 R \tag{4.46}$$

$$M_p(y) = I_\theta \Omega^2 \theta (R - y) + I_T \Omega^2 \theta_T \tag{4.47}$$

where *x* is the chordwise coordinate, *y* is the spanwise coordinate and θ_T is the angle of twist at the blade tip. The torsional moment of inertia of the blade I_θ is small compared to I_T, thus the propeller moment acting on the blade airfoil is negligible compared to the propeller moment acting on the tip mass. Similarly, the centrifugal force on the blade airfoil is negligible compared to the one on the tip mass.

For a general composite laminate, the forces and moments shown on Figure 4.9 are related to reference plane strains and curvatures as (Reference [18])

$$\left\{\begin{array}{c} N_x \\ N_y \\ N_{ss} \\ \hdashline M_x \\ M_y \\ M_{ss} \end{array}\right\} = \left[\begin{array}{c:c} [A] & [B] \\ \hdashline [B] & [D] \end{array}\right] \left\{\begin{array}{c} \epsilon_x^o \\ \epsilon_y^o \\ \gamma_s^o \\ \hdashline \kappa_x \\ \kappa_y \\ \kappa_{ss} \end{array}\right\} \tag{4.48}$$

where [A], [B] and [D], are respectively the extensional, extensional-bending, and flexural stiffness matrices. The B_{xs} term in Equation (4.48) is responsible for the extension-torsion coupling in the direction *x*. As a matter of fact, for a non-zero B_{xs}, a normal force N_x will cause the laminate to twist about the *x*-axis. In order to maximize the twist resulting from the coupling, the term B_{xs} has to be maximized. The matrices [A] and [B] are function of material properties, thickness and

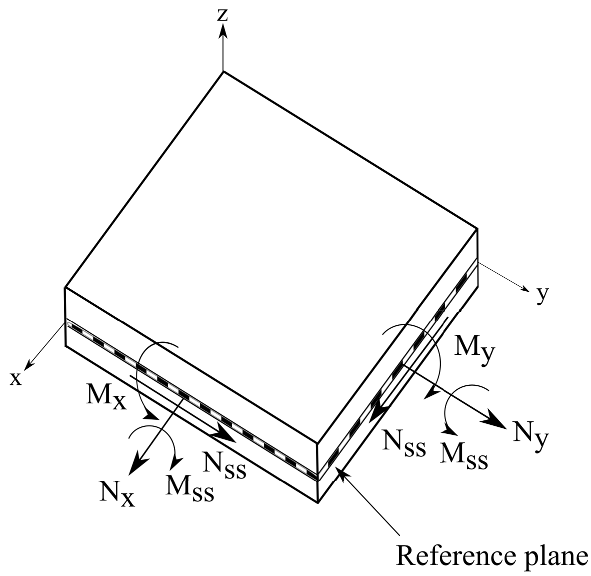

Figure 4.9: Laminated element with force and moment resultants

orientation of the plies and are defined as

$$A_{ij} = \sum_{k=1}^{N} \left[Q_{ij}^{x,y}\right]_k t_k \tag{4.49}$$

$$B_{ij} = \sum_{k=1}^{N} \left[Q_{ij}^{x,y}\right]_k t_k \overline{z_k} \tag{4.50}$$

where the subscript k is summed over the total number of plies and $\left[Q^{x,y}\right]_k$ is the stiffness matrix of the k^{th} layer, expressed in the (x, y) system of coordinates (see Figure 4.10).

As presented in Reference [19], we consider a $[+\theta/-\theta]$ antisymmetric angle-ply laminate , which is known to exhibit strong extension-torsion coupling. If the two layers are considered separately, they are each symmetric with no extension-

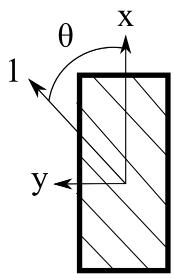

Figure 4.10: Coordinate systems of a generally orthotropic material

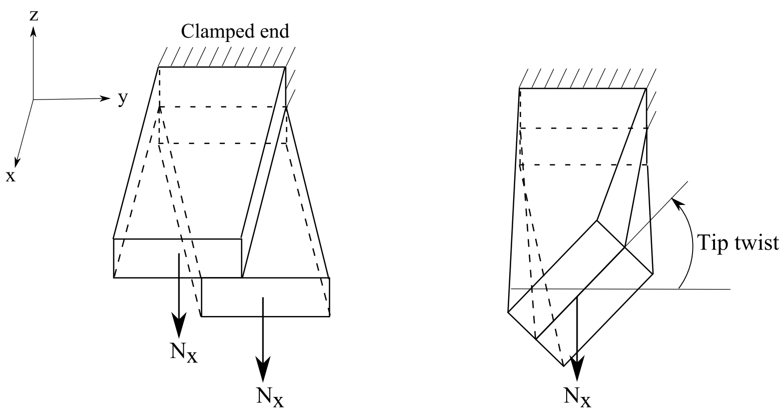

(a) Unbonded plies (b) Bonded plies

Figure 4.11: Extension-torsion coupling mechanism

torsion coupling. However, for both plies, the term A_{xs} is non-zero and is responsible for the extension-shear coupling. The extension-torsion coupling is generated when the two anti-symmetric plies are bonded, as shown in Figure 4.11(a) and 4.11(b). For a given normal tensile force, the largest twist will be obtained when A_{xs} is maximum. Using Equation (4.50), we obtain

$$A_{xs} = t\,Q_{xs} = t\ \Big[Q_{11}\cos^3\theta\sin\theta - Q_{22}\cos\theta\sin^3\theta + Q_{12}\left(\cos\theta\sin^3\theta - \cos^3\theta\sin\theta\right) + 2Q_{66}\left(\cos\theta\sin^3\theta - \cos^3\theta\sin\theta\right)\Big] \quad (4.51)$$

where Q_{11}, Q_{22}, Q_{12} and Q_{66} are related to the material properties of the lamina.

From Equation (4.51), the coupling coefficient A_{xs} can be plotted as a function of the fiber orientation θ (see Figure 4.12). It is observed that the largest twist deformations due to extension-torsion coupling will be obtained for the anti-symmetric angle ply laminate: $[+33^\circ/-33^\circ]$. It can be noted that increasing the number of layers (i.e. $[+33^\circ/-33^\circ]_n$) is unfavorable as the coupling stiffness B_{xs} decreases in inverse proportion to the number of plies, for the same overall thickness of the laminate [18].

In order to decide whether the extension-torsion coupling of a $[+33^\circ/-33^\circ]$ flexible composite blade can balance the unfavorable twist due to the propeller moment acting on the tip mass, the load-deformation Equation (4.48) must be inverted. The result is

$$\begin{Bmatrix} \epsilon^o \\ \hline \kappa \end{Bmatrix} = \left[\begin{array}{c|c} a & b \\ \hline c & d \end{array}\right] \begin{Bmatrix} N \\ \hline M \end{Bmatrix} \quad (4.52)$$

where the matrices [a], [b], [c], and [d] are the laminate compliance matrices. Then, the twist curvature can be expressed as

$$\kappa_{ss} = c_{sx}N_x + c_{sy}N_y + c_{ss}N_{ss} + d_{sx}M_x + d_{sy}M_y + d_{ss}M_{ss} \quad (4.53)$$

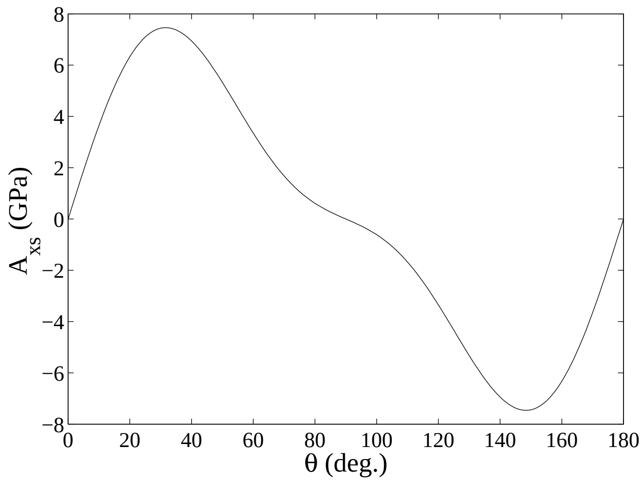

Figure 4.12: Stiffness coefficient A_{xs} as a function of fiber orientation for a unidirectional lamina

Only the terms associated with the propeller moment and the centrifugal force are retained in Equation (4.53). This is justified by the fact that the magnitudes of pitching moments produced by lift and drag are small compared to the one produced by the centrifugal force and the propeller moment. Using Equations 4.44 and 4.45, the twist curvature at the tip of the blade is

$$\kappa_T = c_{sx}\left(m_T \Omega^2 R\right) - d_{ss}\left(I_T \Omega^2 \theta_T\right) \tag{4.54}$$

where, the numerical values for the present study are summarized in Table. 4.1. Finally, the overall twist curvature at the blade tip is

$$\kappa_T = -0.239\left[m^{-1}\right] \tag{4.55}$$

The corresponding angle of twist at the blade tip (assuming a linear twist along the spanwise direction) is

$$\theta_T = -3.1\,[deg] \tag{4.56}$$

Table 4.1: Parameters for composite coupling analysis

Ω $[rad/s]$	θ_T (=θ_{index}) $[deg]$	m_T $[gm]$	R $[cm]$	I_T $[gm.cm^2]$	c_{sx} $[(N.m)^{-1}]$	d_{ss} $[(N.m^2)^{-1}]$
157	22.0	2.15	22.9	4.57	2.624×10^{-3}	6.276×10^{1}

Without consideration of extension-torsion coupling, $\theta_T = -3.6\,[deg]$. As a result, it can be seen that the magnitude of the centrifugal force produced by the tip mass is too small to produce a twist curvature capable of balancing the twist due to the propeller moment. The mass of the tip body cannot be increased as it would decrease the weight efficiency of the rotor . In order to address this problem, the magnitude of the propeller moment must be reduced. In addition, other forms of composite coupling can be investigated. In particular, bending-torsion coupling can be explored in order to stabilize the rotor. However, this requires a refined analysis to identify the lift distribution across the blade span.

4.3.2 Concept B: Tip twist imparted by use of propeller moment

The goal of the concept B is to make use of the propeller moment acting on the tip mass in order to produce an untwisted rotor blade during hover operations. A preliminary step is to design and test a flexible rotor blade whose tip body is a rod secured perpendicularly to the spanwise direction (see blade B2, Section. 5.1.2). Then, maximum efficiency in hover of this blade can be found to occur at a collective pitch angle denoted θ_{index}. The idea is to secure a tip mass (consisting of a solid cylinder oriented perpendicular to the blade span) at the blade tip, at an

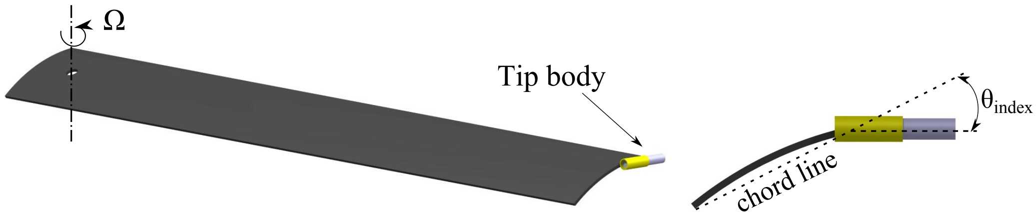

(a) Flexible blade BP (b) Cross section

Figure 4.13: Concept B: Flexible rotor blade BP

angle equal to θ_{index} degrees with respect to the blade chord (Figure 4.13(a) and Figure 4.13(b)). It is expected that while in rotation, the propeller moment acting on the tip body will align its longitudinal axis with the plane of rotation, making the flexible blade untwisted. For future reference, this design is labeled ”Flexible blade BP”.

4.3.3 Concept C: Pitching moment changes introduced by trailing-edge flaps

The third solution investigated to reduce the unfavorable twist distribution involves a trailing-edge flap (TEF). Such systems have been studied in the past for their ability to provide primary flight control as well as vibration and noise reduction [15],[20]. These auxiliary devices are movable elements that permit to change the geometry and aerodynamic characteristics of the blade section. In particular, when a TEF is displaced downward, a nose-down pitching moment is created which twists the blade around its feathering axis. The objective of the present study is to produce a nose-up pitching moment by means of a TEF, capable of balancing the unfavorable nose-down propeller moment.

A preliminary analytical study is carried out in order to determine the di-

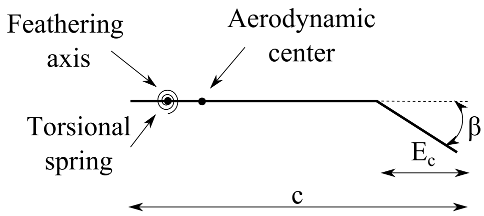

Figure 4.14: Two-dimensional blade section with trailing-edge flap

mensions of the TEF as well as the angle of its deflection such that the flexible blade is untwisted during operations in hover. The two-dimensional case of a blade section with a TEF is considered (Figure 4.14). The lift coefficient and the coefficient of moment about the aerodynamic center can be written in the form

$$C_l = C_{l\alpha}\alpha + \beta\frac{\partial C_l}{\partial \beta} \tag{4.57}$$

$$C_m = C_{m0} + \beta\frac{\partial C_m}{\partial \beta} \tag{4.58}$$

where the aerodynamic constants $C_{l\alpha}$ and C_{m0} are computed for the airfoil with undeflected TEF. From thin-airfoil theory, the coefficients $\partial C_l/\partial\beta$ and $\partial C_m/\partial\beta$ are [21]

$$\frac{\partial C_l}{\partial \beta} = \frac{C_{l\alpha}}{\pi}\left[\arccos\left(1-2E\right) + 2\sqrt{E\left(1-E\right)}\right] \tag{4.59}$$

$$\frac{\partial C_m}{\partial \beta} = -\frac{C_{l\alpha}}{\pi}\left(1-E\right)\sqrt{E\left(1-E\right)} \tag{4.60}$$

where E is the ratio of the flap chord E_c to the total chord c. Theoretical values of the ratios $(\partial C_l/\partial\beta)$ and $(\partial C_m/\partial\beta)$ can be computed for various values of $C_{l\alpha}$ and E and are summarized in Reference [4]. They are plotted on Figure 4.15. In order to maximize the additional nose-up pitching moment produced by the flap, $\partial C_m/\partial\beta$

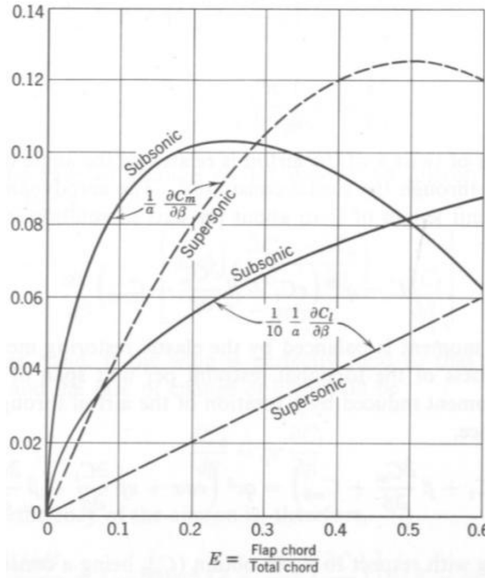

Figure 4.15: $(\partial C_l/\partial\beta)$ and $(\partial C_m/\partial\beta)$ as a function of E, from Reference [4]

has to be maximized. This corresponds to a flap chord to total chord ratio

$$E = 0.25 \tag{4.61}$$

The additional pitching moment resulting from the TEF deflection is

$$(\triangle\ C_m)_{max} = \beta\left(\frac{\partial C_m}{\partial\beta}\right)_{max} \tag{4.62}$$

Setting $(\triangle\ C_m)_{max}$ equal to the pitching moment coefficient associated with the propeller moment acting on the tip body (Equation. (4.47), the required TEF deflection can be computed. The chord of the TEF is deduced from Equation. (4.61). Finally, it should be noted that the dynamic behavior of a flapped airfoil relies on an analysis using a model adapted from Theodorsen's theory [22], but is beyond the scope of this initial simple study.

Chapter 5

Blade fabrication and experimental setup

5.1 Blade design and fabrication

The performance of sets of untwisted, constant chord blades was measured by incorporating them in a two-bladed rotor system. The blades were fabricated in-house and had similar planforms as well as airfoil sections. One set of blades was rigid and the other sets were highly flexible. All the blades were designed such that the center of mass at each cross section was located ahead of the quarter-chord point.

5.1.1 Blade A

A main objective was to decouple bending and torsional flexibility of the blades and to analyze the role played by these two properties on the stability of the rotor. A length of stainless steel tape measure was found to be flexible in torsion but sufficiently stiff in bending, and had a thin circular arc airfoil profile. Accordingly, the blade A consisted of a 8-inch long tape measure in conjunction with a tip mass, oriented perpendicular to the spanwise direction. These blades were fabricated by wrapping uniaxial carbon fibers impregnated with epoxy around a brass tube at the end of the 8-inch length of tape measure. A tungsten rod was then inserted into the brass tube and its chordwise position could be varied. The resulting blades had

Figure 5.1: Flexible blades B1

very sharp leading and trailing edges and were stiff in bending. The non-rotating torsional frequency of this blade was measured to be 10.5 Hz.

5.1.2 Blade B

The flexible composite blade B1 was similar to blade A but was highly flexible both in bending and torsion. It was fabricated using one ply of carbon-fiber cloth oriented $\pm 90°$ with respect to the blade span. The ply was wrapped around a thin-walled brass tube at the tip end, as shown in Figure 5.1, effectively forming a blade two plies thick. A tungsten rod of diameter 0.125 inch and length 0.75 inch was inserted in the brass tube. The carbon-fiber plies were impregnated with a flexible polyurethane elastomer (Freeman 1035) and compressed in a mold . Note that the Young's modulus of the resulting composite is dominated by the carbon-fibers, while the shear modulus is dominated by the polyurethane elastomer.

Blade B2 constitutes an improvement over blade B1 by incorporating a fairing around the tip mass. Aramid fibers (Kevlar©) were found to have a great ability to be wrapped around cylinders with small radius of curvature. Hence, one ply of aramid fibers was wrapped around a brass tube and enclosed between two plies of the $\pm 90°$ carbon-fiber cloth. Figure 5.2(a) shows the blade B2 mounted on the test

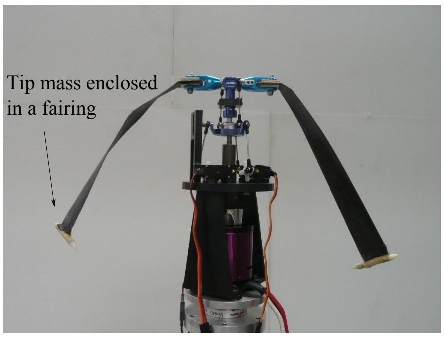

(a) Blades mounted on hover test stand

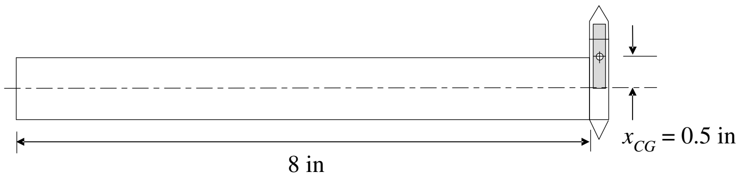

(b) Schematic planform

Figure 5.2: Flexible blades B2

stand and the schematic planform is shown in Figure 5.2(b).

5.1.3 Blade C

Rotor blades C featured an alternate orientation of the tip body, designed to decrease its drag. The axis of the tip mass was parallel to the span of the blade. As the previous blades, these composite blades were fabricated out of carbon fiber using a wet layup process. The laminae were compressed in a mold made out of ABS (see Figure 5.3). A Computed Numerically Controlled (CNC) machine was used to build the molds which allowed to make shapes with very fine contours. The resin employed was either a flexible epoxy resin (Aircraft Spruce AlphaPoxy) for blade C1 or a very flexible polyurethane elastomer (Freeman 1035) for blade C2.

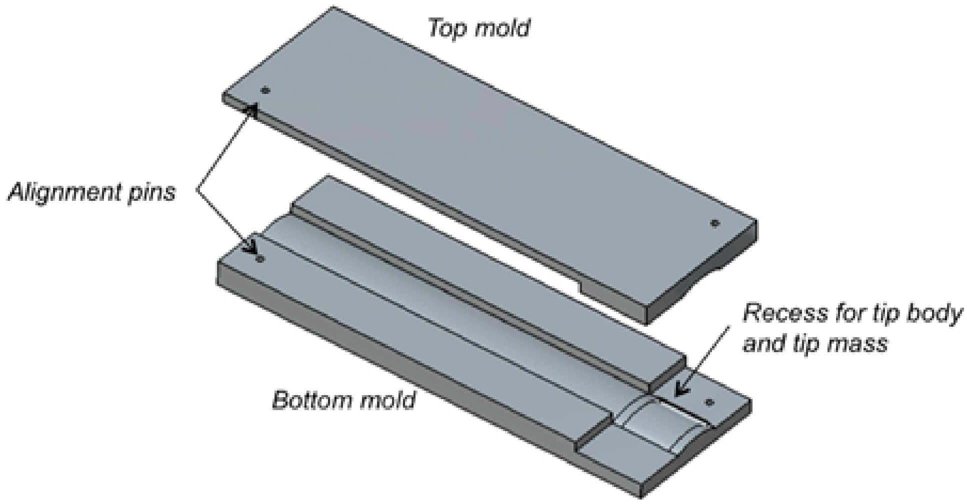

Figure 5.3: Mold for wet layup of blades C

The mechanical properties of the laminates that resulted from impregnating two plies of uniaxial carbon-fiber, with these matrices were determined through a set of tensile tests and are given in Table 5.1. Note that the elastic moduli of the composite with the Alphapoxy matrix are higher than that of the Elastomer matrix. Hence, blades of different stiffnesses could be fabricated by varying the matrix. Due to the extreme flexibility of these blades, none of their non-rotating frequencies could be measured.

In order to fabricate the rotor blades corresponding to design C, the tip mass was wrapped parallel to the span of the blade. One ply of aramid fibers held the tip body and was enclosed between two plies of carbon-fiber cloth. The blades C1 were torsionally soft but stiff in bending, while the blades C2 were extremely soft both in torsion and in bending (see Figures 5.4(a) and 5.4(b)). Both these 2 blades had the same planform, shown in Figure 5.5. The set of blades C2

Table 5.1: Mechanical Properties of the composite materials used in flexible blade fabrication

	Carbon Fiber / Elastomer	Carbon Fiber / $Alphapoxy^{©}$
Tensile modulus E_1 (GPa)	20.3	25.0
Tensile modulus E_2 (GPa)	0.1	0.1
Shear modulus G_{12} (GPa)	0.46	1.54
Poisson ratio	0.3	0.3
Mass per unit area (gm/cm^2)	0.043	0.037

(a) Flexible blades C1

(b) Flexible blades C2

Figure 5.4: Blades C1 and C2 mounted on hover test stand

impregnated with elastomer were flexible enough to be rolled up into a cylinder. On the contrary, composite blades C1 made out of Alphapoxy were found to be too stiff in bending to be rolled up. This observation led to the design of blade C3. In order to transfer twist deformations from the root to the tip of the blade, while keeping its ability to roll up into a cylinder, these blades were fabricated using the very flexible carbon-fiber/elastomer laminate at the root, and carbon-fiber/Alphapoxy composite material at the tip of the blade. A planform schematic of blade C3 is shown in Figure 5.6.

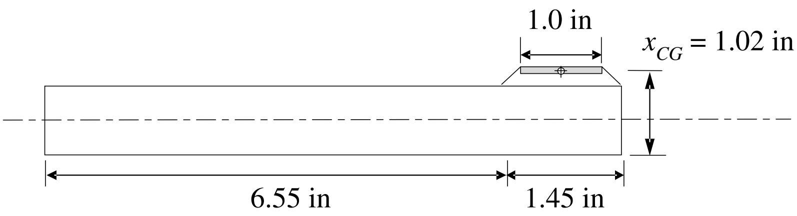

Figure 5.5: Schematic planform of blade C1 and blade C2

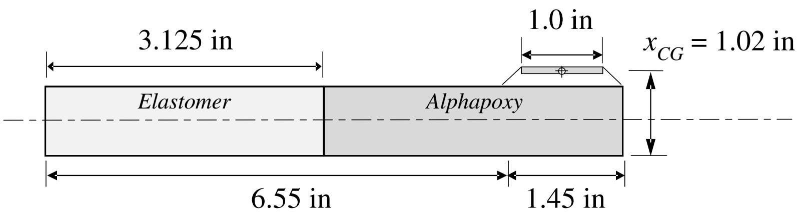

Figure 5.6: Schematic planform of blade C3

Finally, blade C4 was identical to blade C1 but had its fibers oriented $\pm 45°$ with respect to the blade span. It was found that this flexible blade could easily be rolled up.

5.1.4 Blade BP

The blade BP was an iteration of blade B1 and was designed in order to address the problem of twist deformation. A schematic planform was shown previously (see Figures 4.13(a) and 4.13(b)). A 0.002-inch thick brass rectangular plate, having a camber equal to 7.5 %, a chord length of 0.3 inch and a length of 0.6 inch was inserted at the leading edge of the mid-ply of the composite laminate. The resulting blade is shown mounted on the hover test stand in Figure 5.7.

The maximum efficiency of blade B1 was obtained at a collective pitch an-

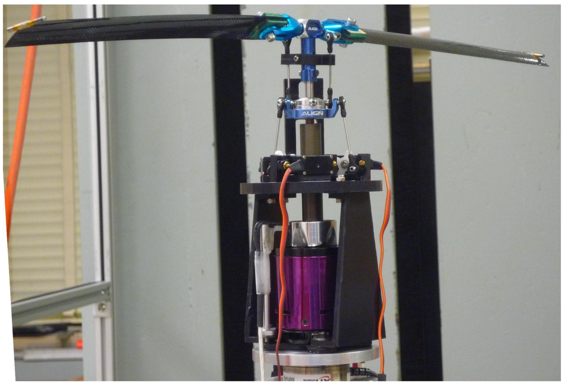

Figure 5.7: Flexible blades BP mounted on hover test stand

gle of 22 degrees (Section 6.2). Accordingly, a thin-walled brass cylinder was soldered to the plate, such that it made an angle of 22 degrees with the blade chord. A mold was used in order to make the assembly process repeatable with accuracy. A tip mass, consisting of a $3/32$ inch diameter tungsten rod of length 1 inch was inserted inside the brass tube and its chordwise position could be varied. The entire assembly was securely attached to the flexible blade by using a high strength resin epoxy. In particular, it had been verified that the tensile shear strength of the epoxy was greater than the shear stresses induced by the centrifugal force applied on the tip object. Table 5.2 summarizes the properties of the flexible blade BP.

5.1.5 Blade CF

The concept of blade CF relied on the design of blade C4 where the tip mass was a tungsten rod aligned with the span of the blade. A trailing-edge flap was added and mounted at the trailing-edge, aft of the tip body (Figure 5.8).

This flexible blade was fabricated in two parts, shown in Figure 5.9. The

Table 5.2: Flexible blade BP parameters

Rotor radius, $[m]$	0.229
Chord, $[m]$	0.024
Thickness, $[mm]$	0.25
Camber, %	7.5
t/c ratio, %,	1.0
Airfoil mass, $[g]$	2.00
Attachment feature mass, $[g]$	0.25
Tip mass, $[g]$	2.05
Total blade mass, $[g]$	4.30

blade airfoil was composed of two $[+45/-45]$ Carbon/$AlphaPoxy^{©}$ plies. Between these layers, a $Kevlar^{©}$ sheet enclosed the tip mass as well as a polymer foam core. The composite lay-up was compressed inside a mold and cured at room temperature. The TEF consisted of 6 layers of a $[0/90]$ Carbon/epoxy lamina. The resulting composite laminate was rigid compared to the blade airfoil. Two spring steel supports were inserted at the mid ply. The angle between the chord of the flap and the supports was set at the desired value and the flap was inserted inside the

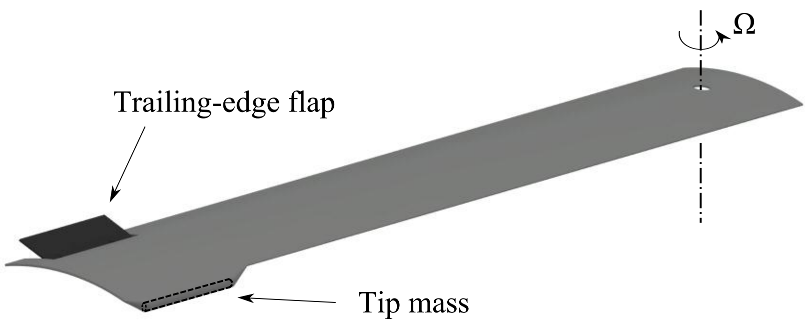

Figure 5.8: Flexible blade CF

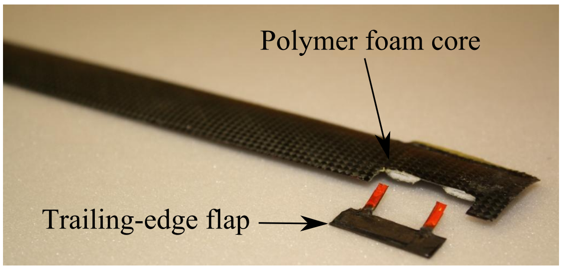

Figure 5.9: Fabrication of flexible blade CF

blade core.

Because of the geometrical complexity and the inhomogeneity of the materials, the center of mass of the blade was computed numerically. The blade CF was designed such that the center of gravity at each section was located ahead of the $1/4$ chord. Finally, Table 5.3 shows the design parameters chosen for the flexible rotor CF.

Table 5.3: Flexible blade CF parameters

Rotor radius, $[m]$	0.229
Airfoil chord, $[m]$	0.024
TEF chord, $[m]$	0.008
TEF span, $[m]$	0.025
Airfoil thickness, $[mm]$	0.4
Camber, $\%$	7.5
t/c ratio, $\%$,	1.7
Airfoil mass, $[g]$	2.45
TEF mass, $[g]$	0.25
Tip mass, $[g]$	2.05
Total Blade mass, $[g]$	4.75

5.1.6 Rigid blade

The rigid blades were fabricated using two plies of carbon-fiber cloth, oriented $\pm 45^\circ$ to the blade span. The plies were impregnated with a conventional room-temperature cure resin and were compressed in a mold. The resulting blades were stiff in torsion as well as in bending, and had the circular arc sectional profile imparted by the mold.

5.1.7 Blade matrix - Summary

Table 5.4: Blade design matrix

Design	Schematic planform	Material	Rotor radius, [in]	Chord, [in]	Thickness, [in]	Camber, %	t/c ratio, %	Airfoil mass, [g]	Tip body mass, [g]	Total blade mass, [g]
A	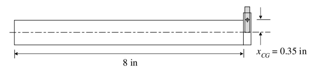	Spring steel	9	0.7	0.007	12	0.01	5.82	4.58	10.4
B1		Carbon fiber/ Elastomer	9	0.7	0.026	5.5	3.6	4.89	4.65	9.54
B2	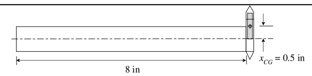	Carbon fiber/ Elastomer	9	1	0.03	7.5	3	5.85	4.40	10.25
C1	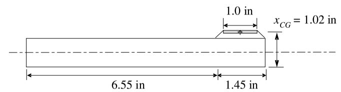	Carbon fiber/ Alphapoxy	9	0.9	0.015	7.5	1.7	2.20	2.15	4.35
C2		Carbon fiber/ Elastomer	9	0.9	0.020	7.5	2.2	3.10	2.15	5.25
C4		Carbon fiber/ Alphapoxy ($\pm45°$ wrt. span)	9	0.9	0.015	7.5	1.7	2.35	2.15	4.50
C3	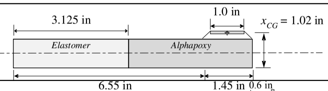	Carbon fiber/ Elastomer/ Alphapoxy	9	0.9	0.013	7.5	1.4	2.00	2.15	4.15
BP	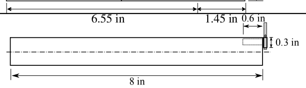	Carbon fiber/ Alphapoxy	9	0.95	0.010	7.5	1.1	2.00	2.30	4.30
CF	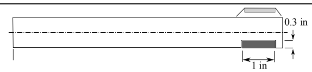	Carbon fiber/ Alphapoxy	9	0.95	0.016	7.5	1.7	2.45	2.30	4.75
Rigid blade	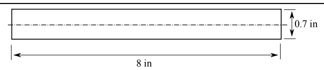	Carbon fiber/ Resin epoxy	9	0.7	0.025	5.5	3.6	4.65	*N/A*	4.65

5.2 Experimental setup

The performance of the blades in hover was measured on a test stand designed and built inhouse, shown in Figure 5.10. The two-bladed rotor hub was mounted directly on a brushless outrunner DC motor. The motor (Hacker A50 16S) was chosen to have a high torque and low speed constant so that it could directly drive a rotor of diameter up to 0.6 m, at a tip speed of up to 135 m/s, without the need for a gearbox. A swashplate assembly operated by three high speed digital servos allowed precise adjustment of the rotor collective and cyclic pitch angles. The motor and rotor assembly was mounted directly on a six component strain gage load cell (ATI Mini40E), with a full scale rating of 5 lbs in the thrust direction. A magnetic pickup provided a 1/rev pulse, which was used to measure the rotational speed, as well as to perform synchronous averaging of all the signals. This pulse was also used to trigger a strobe light to illuminate the rotor and enable photography of the blade shape in flight. Hence, stability boundaries as well as blade deformations were observed visually. Data was acquired by a National Instruments CompactDAQ system with a custom virtual instrument programmed in Labview. The quantities measured were the rotor forces and moments in the fixed-frame, rotational speed, motor voltage and motor current.

5.3 Test matrix

5.3.1 Hover test

The hover testing was performed at a constant rotor speed of 1500 RPM. The rigid and flexible blades were tested over a range of collective pitch angles

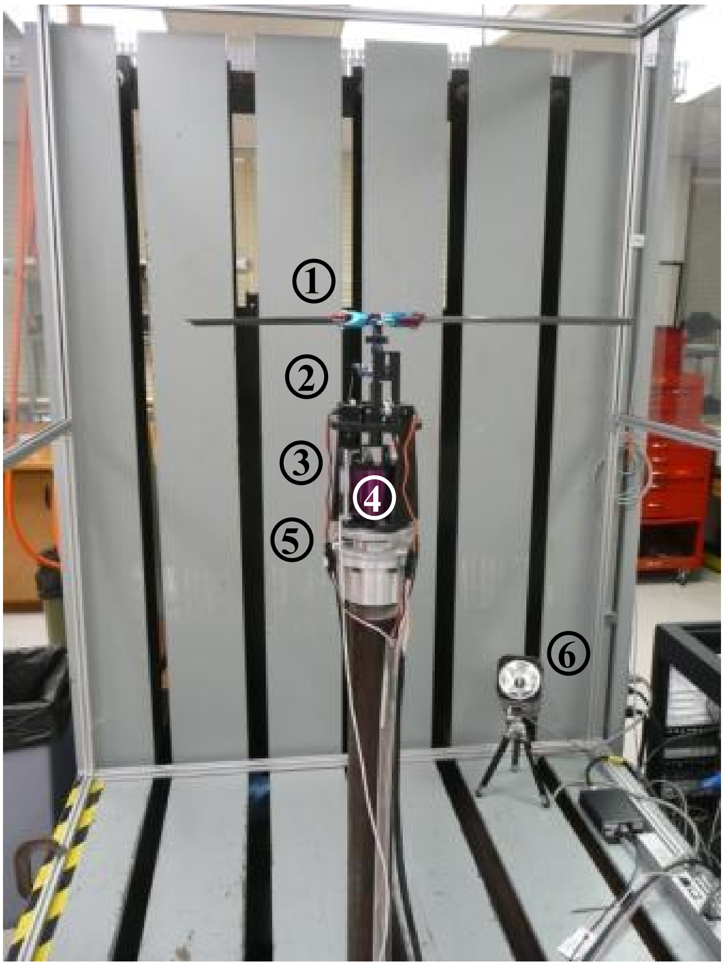

1 Rotor hub
2 Swashplate
3 Hall sensor
4 DC brushless motor
5 6-component load cell
6 Stroboscopic light

Figure 5.10: Hover test stand

from 0 degree to 30 degrees. The goal of the hover tests was to measure the thrust generated by the flexible blades as a function of the collective pitch and to measure the efficiency of the rotors in terms of hover Figure of Merit. The region of stable operation of the blades was first identified. Previous studies relied on audible changes in noise or vibration to determine the onset of instability. The present study used the strobe light to visually observe the blade deformation in flight. In this way, flutter oscillations of an unstable blade could clearly be observed, while no blade motion was discernible for the stable blades. It was noted that in several cases, there was no audible change in noise in spite of visual evidence of instability. No data was collected in the cases where the rotor was unstable.

In order to compare the effect of the trailing-edge flap deflection on the rotor performance, two sets of flaps were tested. The angle β between the flap and the blade chord was respectively equal to -10 degrees and -20 degrees. From the experimental data, the thrust coefficient and Figure of Merit were computed and compared to that of an identical flexible rotor non-equipped with a TEF.

5.3.2 Forward flight test

Forward flight experiments were conducted in a subsonic, closed-circuit, open test section wind tunnel. The hover test stand was installed in the open test section, as shown in Figure 5.11. The dimensions of the test section were 36in x 22in x 30in. Air flow was provided by a constant running 75HP motor. Test section velocity was controlled by a variable clutch located between the fan and the motor shaft. The minimum and maximum tunnel velocities were 5 ft/s and 80

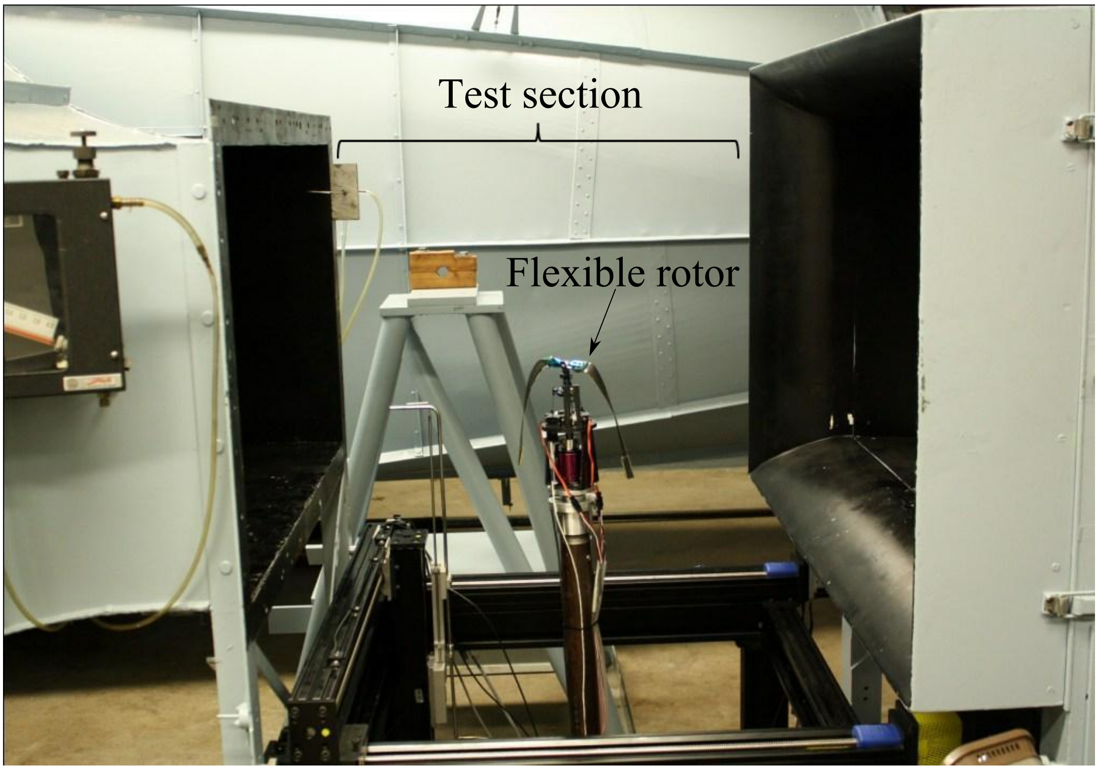

Figure 5.11: Forward flight test setup

ft/s respectively. The rotors showing the best hover performance were chosen for the forward flight tests. The rotor loads were measured at at least three different collective pitch settings and three advance ratios. At each setting, the rotor was trimmed using the collective and cyclic pitch inputs so that the thrust was constant and the roll and pitch moments at the rotor hub were zero. In addition, the rotor shaft was tilted forward by 1.5 degrees to ensure rotor trim over the entire range of advance ratios tested.

Chapter 6

Results and discussion

6.1 Aeroelastic stability

The flexible rotor concepts presented in this paper were designed such that the center of gravity at each blade section was located forward of the quarter chord point. This condition was shown to be sufficient for ensuring pitch-flap flutter and divergence stability, regardless of the rotor speed [1, 2, 12]. However, experimental data showed that this stability criterion was invalid for the types of blades presented in this study. As mentioned earlier, onset of stability or instability was inspected visually in this study. The sharp transition between a stable regime and unstable operations of the rotor is shown on Figure 6.1. The photographs were taken using a long exposure, resulting in the blade position being recorded over multiple rotor revolutions. The blurred image indicates that the corresponding regions of the blade are undergoing motion at a frequency higher than 1/rev.

It appeared that pitch-flap flutter instability of the flexible rotors was not only dictated by the rotational speed of the rotor, but also by the collective pitch angle. Figure 6.2 shows the pitch flutter stability boundary of blade A. For a collective pitch angle greater than 7.5 degrees, the rotor was always stable. The stability boundary of blade C1 with the rate of rotation and collective pitch angle as param-

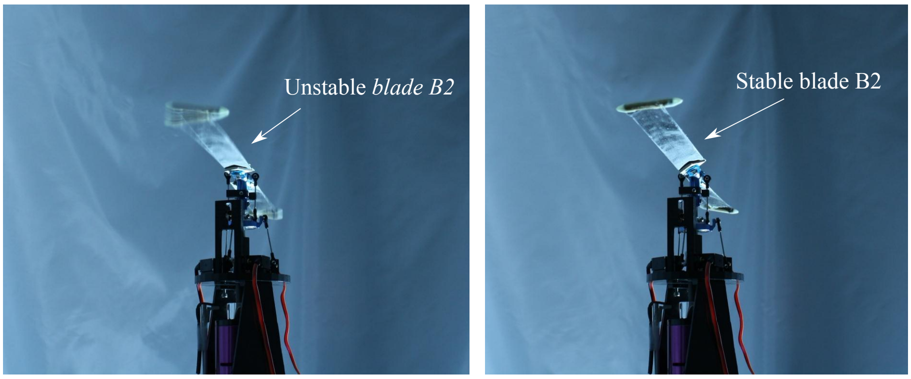

(a) Unstable blade B2, 1500 RPM, $\theta_o = 0°$. (b) Stable blade B2, 1500 RPM, $\theta_o = 10°$

Figure 6.1: Pitch flutter and stable operations of the blades B2. Blurred image shows higher frequency flutter

eters followed the same trend. It should be observed that previous analyzes on the aeroelastic stability of flexible blades assumed infinitely small torsional and bending stiffnesses. This hypothesis implies that the blade cannot sustain its own weight in the non-rotating condition, which is invalid for the designs A and C1. The blades C2 fabricated using flexible elastomer approximated an infinitely flexible rotor. Experimentally, it was observed that the blade was unstable for collective pitch angle in the range 0 degrees to 25 degrees and then very stable for very high collective pitch angles, above 30 degrees.

Stability boundaries of the flexible rotors BP and CF were also investigated. The blades BP were found to be stable for any collective pitch angle greater than 11 degrees. This observation coincides with the one previously made: the flutter instability identified is a low pitch phenomenon. An important result is that the flexible rotor blades CF were found to be stable for any value of collective pitch

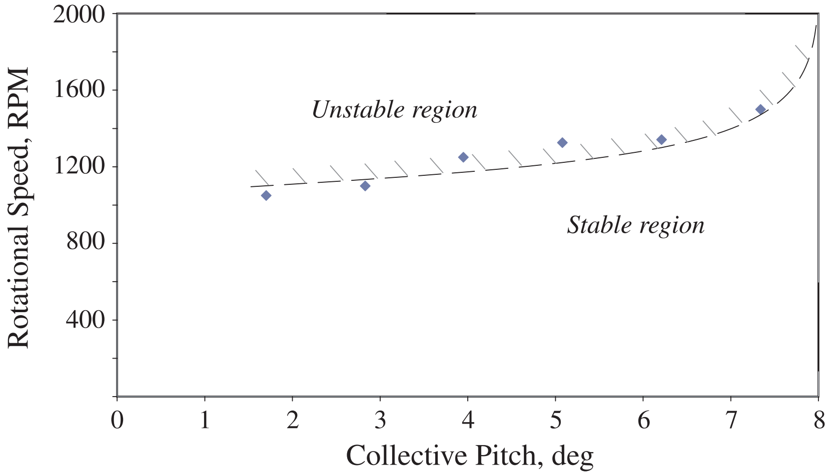

Figure 6.2: Stability boundary of rotational speeds and collective angles - Blade A

angle. This means that the introduction of the TEF alleviated the flutter instability.

Existing analytical studies of instability are unable to capture the behavior of the flexible blade, especially at the scale of a micro-helicopter. Winston [1] assumed large rotors with slow rotating rates while Goldman [12] assumed infinite flexibility. More recently, a comprehensive rotor aeromechanics code (UMARC [23]) that has been validated for full-scale helicopters, was used in order to predict the stability boundaries of a flexible rotor. In general, it has not been possible to create a model that matched the performance of a micro-helicoter. In order to accurately model the stability and behavior of a flexible micro-helicopter rotor blade, a refined comprehensive aeromechanics code focused on large displacements and very low material stiffness has to be developed from first principles.

6.2 Rotor performance in hover

The objective of the first series of tests was to compare the effect of different tip body designs and locations on the performance of the flexible rotors.

Figure 6.3 shows the thrust coefficient in hover as a function of collective pitch angle. In helicopter analysis, this coefficient is formally defined as

$$C_T = \frac{T}{\rho A V_{tip}^2} = \frac{T}{\rho A \Omega^2 R^2} \tag{6.1}$$

where A is the rotor disk area and V_{tip} is the blade tip speed, ΩR. Stall is indicated by the change in the slope of the thrust coefficient curve. It can be noted that the stiffer the blade is in torsion, the lower the collective pitch at which stall occurs. Hence, the lowest stall angle occurred for the rigid blades, at around 19 degrees. The composite *blade C1*, impregnated with AlphaPoxy was stiffer than the elastomer blades and stalled at a very high collective pitch angle (40 degrees). The extremely flexible elastomer blades do not indicate any onset of stall. The performance of the flexible blades was measured up to a collective pitch of 50 degrees. Although the thrust coefficient was still increasing with collective pitch at that angle, the Figure of Merit showed a decrease in the rotor efficiency. Therefore, measurements were not performed at collective pitch angles greater than 50 degrees. This behavior has already been underlined by Winston [1] . Because of the high twist angles induced in the flexible blades, the outboard section of the blades that is responsible for the greatest percentage of thrust remains unstalled. Figure 6.4 shows the deformation of blades C3 at high pitch angles. Because the largest twist angle is located at the root, replacing the elastomer outboard portion

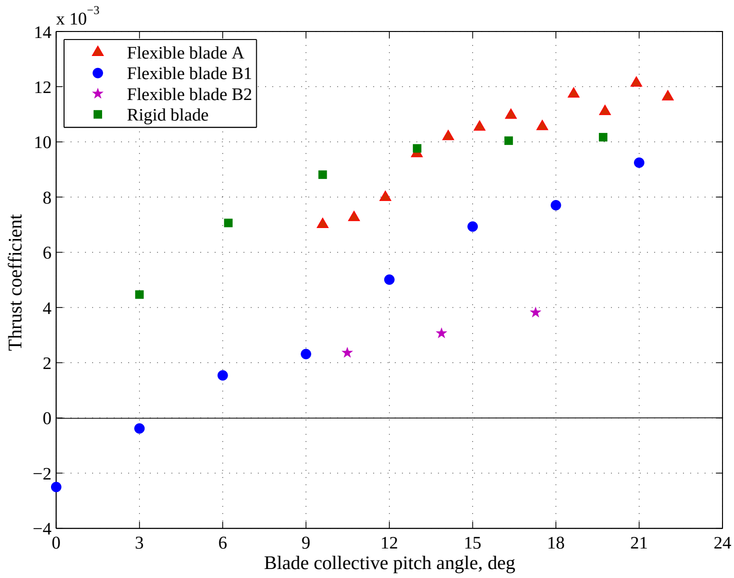

(a) Blade Designs A's, B's and rigid

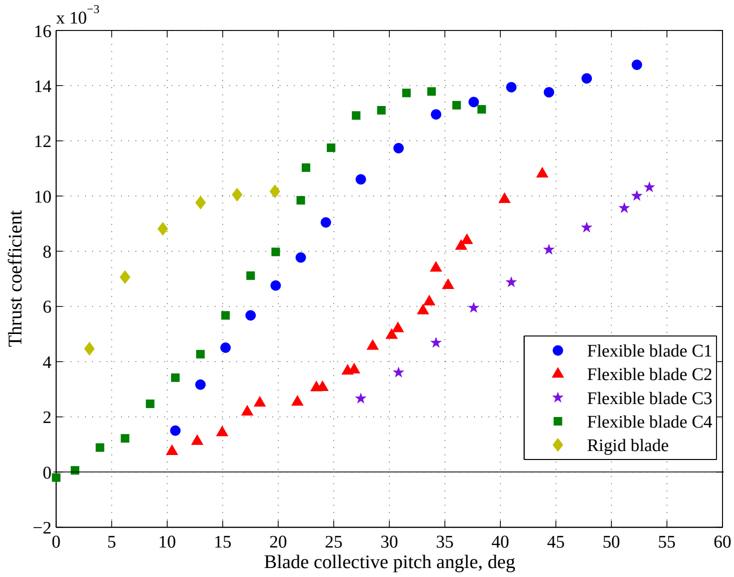

(b) Blade Designs C's and rigid

Figure 6.3: Comparison of thrust coefficients of rigid and flexible rotors at 1500 RPM

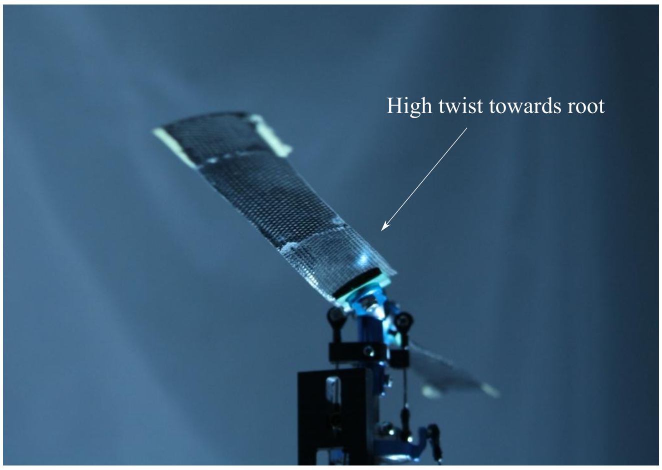

Figure 6.4: Stable blade C3. Note high twist angle at the inboard section of blade

by a stiffer AlphaPoxy laminate did not increase the thrust coefficient of the blade. Consequently, in terms of thrust coefficient, the designs C1 and C4 which combine carbon fiber with a flexible resin gave the best performance. In the case of the flexible blades, forces and moments were not measured for collective pitch angles below 10 degrees, because the rotors were not stable at these angles at 1500 RPM. However, the slope of the thrust coefficient curves indicates that if the blades had been stable, they would have generated a negative thrust. This result is attributed to the nose-down torsional moment caused by the weight of the tip mass, resulting in a net negative twist of the rotor blade and a negative angle of attack at the outboard locations.

Figures 6.5 and 6.6 shows the Figure of Merit of each rotor, as a function of blade loading . As expected, the rigid rotor blades are the most efficient and their maximum FM is approximately 0.50 for a blade loading of 0.15. The best FM for a flexible blade is achieved by the design C4 (carbon-fiber/AlphaPoxy, oriented

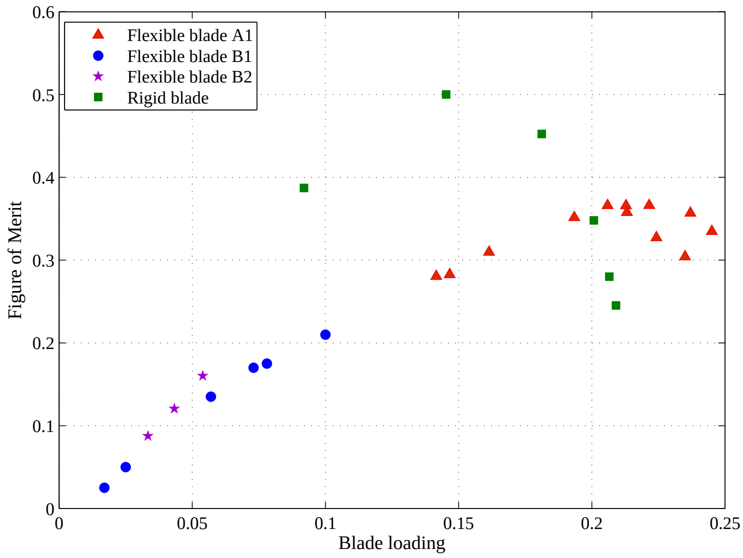

Figure 6.5: Figures of Merit of blade designs A's, B's and rigid, at 1500 RPM

$\pm 45°$ with respect to the span) and is equal to 0.41. This value is twice the maximum Figure of Merit obtained for the blades B1 and B2. This enhancement comes mainly from the change in material rather than the change in planform. Indeed, the maximum FM of the blade C2 (carbon-fiber/elastomer) is only 0.25, representing an increase of only 0.05 compared to the blades B1. While the blade C3 (made out of both elastomer and AlphaPoxy) did not provide any improvement in terms of thrust coefficient, it is seen to be more efficient than the blade constructed with only an elastomer matrix, and reaches a maximum FM of 0.3.

These hover test results demonstrated that micro-helicopter blades fabricated with a flexible resin such as the AlphaPoxy offer a good compromise between rigid rotor blades and extremely flexible blades made out of elastomer. The perfor-

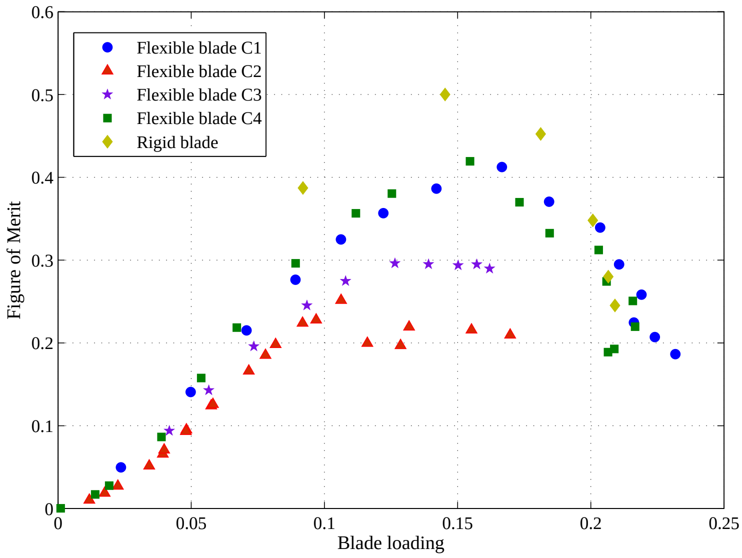

Figure 6.6: Figures of Merit of blade designs C's and rigid, at 1500 RPM

mance of such a rotor is close to that of a rigid rotor and it has sufficient flexibility to be impact resistant as well as amenable for a varying rotor diameter design.

The objective of the second series of hover tests was to evaluate the potential benefit on the performance of the designs BP and CF.

Figure 6.7 shows the Figure of Merit of the flexible blade BP. It is compared to the Figure of Merit of the identical flexible rotor blade whose tip mass is aligned with the chord of the airfoil (design B1). The Figure of Merit of a conventional rigid rotor having the same planform is also plotted. It can be seen that the index angle between the tip mass and the chord has a favorable effect on the rotor efficiency in hover. The maximum Figure of Merit of the present design is equal to 0.51 for a blade loading of 0.14, which is more than twice that of the design B1.

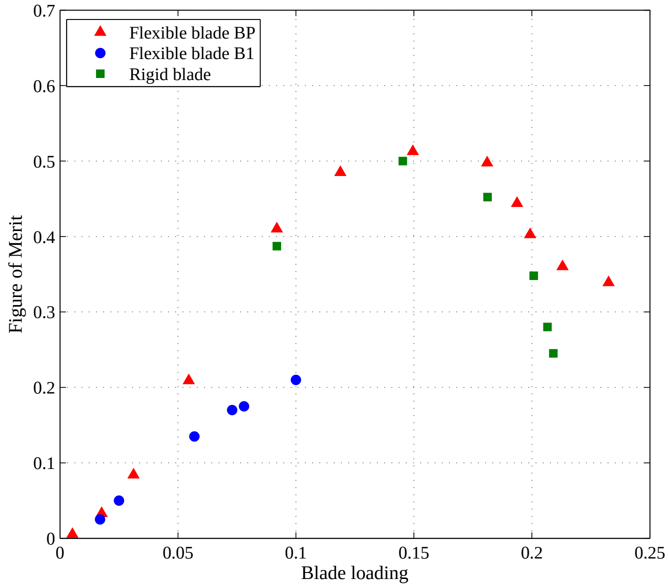

Figure 6.7: Figure of Merit of the flexible blade BP

This improvement is related to the control of the twist along the blade span, which almost vanishes at optimum operation of blade BP. The maximum Figure of Merit is obtained at a collective pitch angle of 16 degrees. Thus, a new iteration where the index angle is equal to 16 degrees has to be made in order to totally eliminate the twist due to propeller moment.

Figure 6.8 shows the blades BP mounted on the whirl test stand. It can be observed that in hover, the longitudinal axis of the tip mass lies in the plane of rotation of the rotor. As a result, the flexible blades are untwisted even at high collective pitch angle.

Finally, the blade CF was tested and compared to blade C4 and a rigid blade.

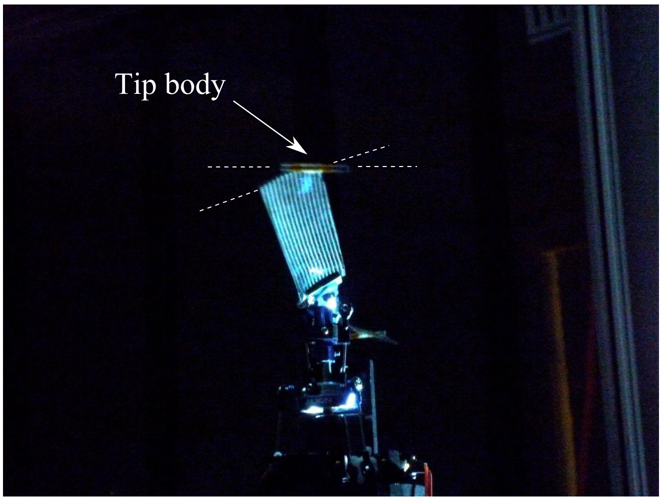

Figure 6.8: Blade BP at $\theta_0 = 22°$

Figure 6.9(a) shows the thrust coefficient as a function of collective pitch angle. The TEF being deflected at negative values of β (Figure 6.10) is responsible for a downward force on the airfoil, which results in a decrease of C_T. This also appears in the fact that negative thrust coefficients are produced at low collective pitch angles.

The Figures of Merit of the flexible rotors tested in hover are shown in Figure 6.9(b). It can be observed that the addition of the TEF induced a loss in efficiency. The pitching moment created by the TEF was not large enough to produce the nose-up twist required to balance the propeller moment. As a result, there is no improvement of the performance of the flexible blade with no flap (blade C4). Instead, the decrease in thrust produced by the flap (deflected upward) contributes to a poorer Figure of Merit.

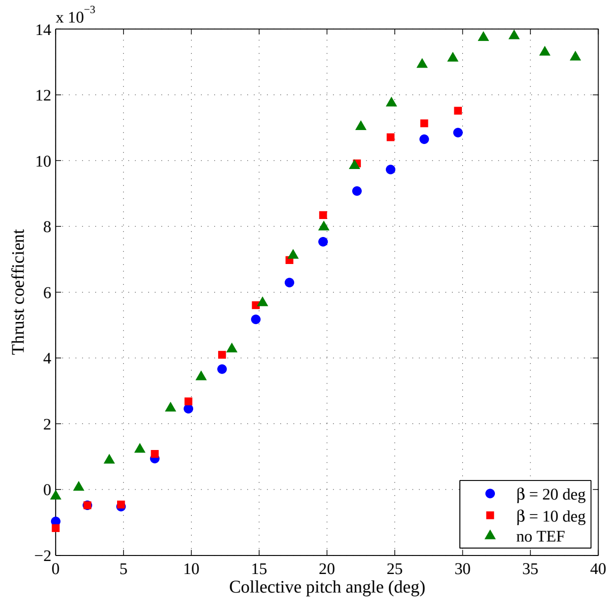

(a) Thrust coefficient at N=1500 RPM

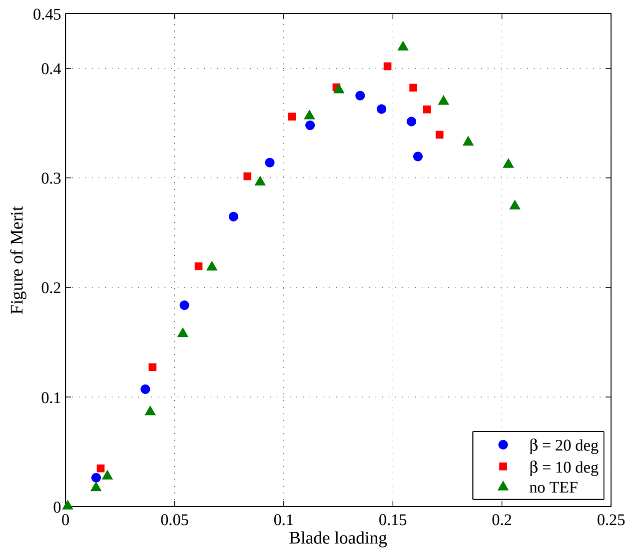

(b) Figure of Merit at N=1500 RPM

Figure 6.9: Performance of the flexible blade CF

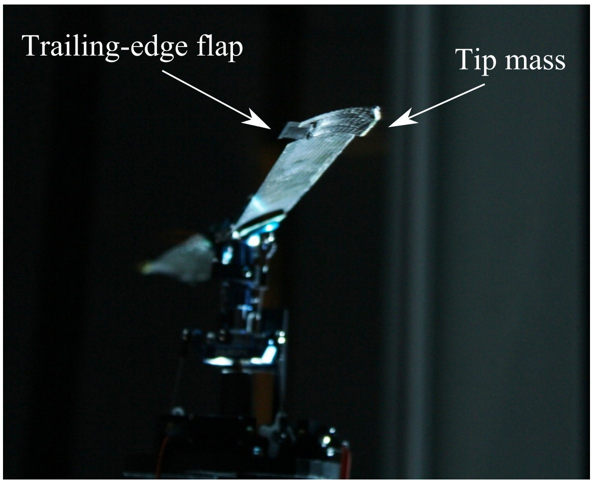

Figure 6.10: Flexible blade CF in hover

6.3 Rotor performance in forward flight

Based upon the performance in hover, the flexible rotor design C1 and design C2 were selected for forward flight testing. For each rotor, data was collected at three values of thrust coefficient corresponding to efficient operation in hover. At an advance ratio of 0.05, 0.1, 0.15 and 0.25, collective pitch angles were set in order to attain the constant thrust defined above, and the rotor was trimmed to get zero hub moments. Data were collected to plot the power curve of each rotor at constant thrust coefficient, for various advance ratio. A constant rotational speed of 1500 RPM was maintained for all tests.

A key observation from the forward flight testing of a flexible rotor is that the incident velocity does not adversely affect its stability. Indeed, it was observed that rotor blades stable in hover remained stable at all advance ratios. Blade design C1 and design C2, which proved to be the most efficient in hover were tested in forward flight and their performance was compared to that of a rigid rotor. Figure 6.11 shows the variation of the power coefficient with respect to advance ratio, at constant thrust. It can be seen that the power required by the flexible blades is on the order of twice the power required by the rigid rotor to operate. Because of the very large twist deformation at the blade root, the inboard portion of the blade produces a lot of drag. Consequently, the profile power increases and so does the total power of the rotor. It should be noticed that in hover, this increase in profile power is less significant because the inboard section where the drag is produced coincides with area of low dynamic pressure.

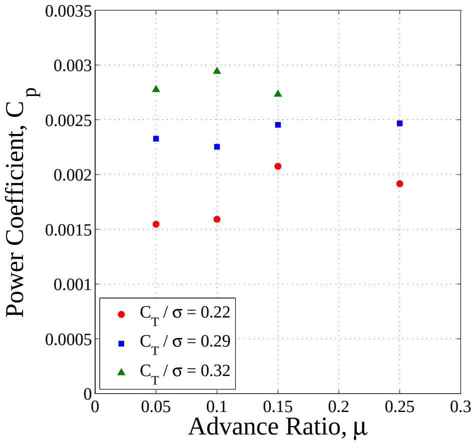

(a) Blade design C1

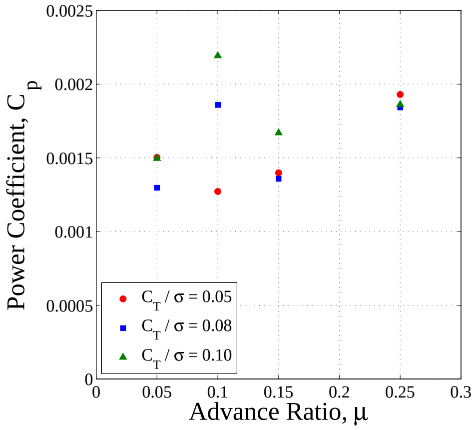

(b) Blade design C2

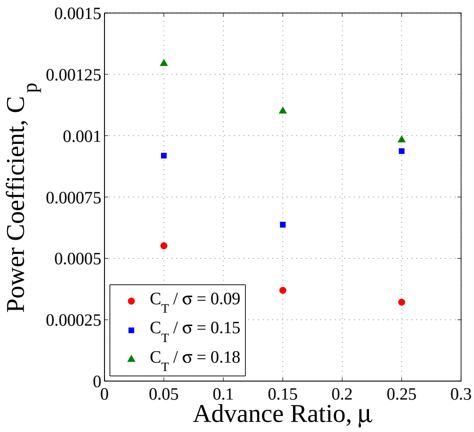

(c) Rigid blades

Figure 6.11: Comparison of power coefficients for rigid and flexible rotors at constant thrust coefficients

Chapter 7

Summary and conclusions

Rotors with extremely flexible composite blades were fabricated and tested in hover and forward flight. The goal was to develop blades so flexible that they could be rolled up and stowed in the rotor hub. The design of the rotor blades was focused toward application on a micro-helicopter. Accordingly, the blades had a circular arc airfoil section with 7.5% camber, untwisted, constant chord planform, and a span consistent with a rotor diameter of 18 inches. A tip mass was used to stabilize the flexible rotor.

A systematic experimental investigation was conducted to define the planform, mass distribution and materials of an efficient flexible rotor. Flexible rotor blades of different stiffnesses were fabricated, and tested. The experimental data indicated that the most efficient design of this first phase of testings incorporated a tip body comprised of a 1-inch long tungsten rod aligned with the spanwise direction of the blade and located at the leading edge. The tip body was placed so that the overall center of gravity of the blade was ahead of the quarter chord point. While previous analytical studies related to extremely flexible rotors had concluded that rotor stability was independent of the rotational speed, it was found experimentally that both the collective pitch angle and the rotational speed had a significant effect on the stability of the rotor.

The mass of the most efficient design (design C4) was 4.35 grams (tip mass included) which was of the same order of magnitude as the rigid blade. Stall of the flexible rotor was observed to occur at a very high collective pitch angle of 40 degrees. At that point, the inboard section of the blade was highly twisted. A maximum Figure of Merit of 0.41 was measured. In comparison, a rigid rotor of the same diameter and solidity had a maximum Figure of Merit of 0.5. The poor efficiency of the flexible blades was attributed to an unfavorable twist distribution along the blade span, caused by the combination of the propeller moment and the gravitational force acting on the tip body. Accordingly, approaches to passively tailor the spanwise twist distribution were investigated.

In a first approach, extension-torsion composite coupling was investigated in order to make use of the centrifugal force produced by the tip mass to generate nose-up twist deformations. It was found that a $[+33°/-33°]$ composite laminate generates the largest twist curvature for a given normal force. However, the magnitude of the centrifugal force is too small to balance the negative twist curvature due to the large propeller moment. The final result was a twisted blade whose twist angle at the blade tip was $\theta_T = -3.1\ deg$.

The objective of the second concept was to make use of the propeller moment acting on the tip mass in order to produce an untwisted rotor blade during hover operation. A tungsten rod oriented perpendicularly to the blade span was secured at the blade tip, and its longitudinal axis made an angle of 22 degrees with respect to the blade chord. It was observed that in hover, the longitudinal axis of the tip body lied in the plane of rotation of the rotor, yielding a pitch angle at the tip of 22 degrees. As a result, for an equal collective pitch angle, the rotor was untwisted. This had a favorable effect on the performance. A maximum Figure of Merit of 0.51 was computed which is more than twice that of a similar rotor with no tip pitch control. The blade loading at maximum Figure of Merit was equal to 0.14. Finally, the flexible blades were found to be stable for any collective pitch angle greater than 11 degrees.

The goal of the third approach was to design a trailing-edge flap capable of generating pitching moments at the blade tip and balancing the propeller moment acting on the tip mass. According to a two-dimensional analysis, a TEF was fabricated and mounted on a flexible blade whose tip mass was aligned with the spanwise direction. The rotor was tested in hover for various values of flap deflections. It was found that the performance of the rotors equipped with TEF were poorer than that of identical blades with no flaps. The pitching moment imparted by the TEF was not sufficient to balance the propeller moment on the tip body, resulting in a highly twisted blade. At the same time, the TEF deflected upward (i.e. negative values of β) was responsible for a downward force on the airfoil. As a result, the maximum Figure of Merit of the flexible blade with TEF was smaller than that of the same blade with no flap. An important result was that the addition of the TEF yielded a stable rotor for any value of collective pitch angle.

Finally, forward velocity was observed to increase the stability of a flexible rotor. Forward flight test measurements pointed out that the power coefficient for the flexible blade was twice that of a rigid rotor, where advance ratio and thrust coefficient were kept constant. This was attributed to the very high angles of attack induced by the twist at the inboard sections. While the inboard sections of the rotor correspond to a region of low dynamic pressure in hover, this is no longer true in forward flight and the profile power term becomes dominant.

Future plans involve the development of a comprehensive aeromechanics analysis capable of modeling large deformations and blades with very low stiffness. The analysis will be validated with the experimental results obtained in the present study. In addition, the design of a trailing-edge flap will be refined by developing a BEMT model of the flexible airfoil. Finally, other forms of composite material coupling, such as bending-torsion coupling, will be investigated, in order to extend the stability boundaries of extremely flexible rotor blades.

Appendix

Appendix 1

Blade moments of inertia

$$
\begin{aligned}
I_\beta &= \int_e^R (y-e)^2 \, dm \\
I_b &= \int_e^R y^2 \, dm \\
I_x &= \int_e^R x_I \, y \, dm \\
S_\beta &= \int_e^R y \, (y-e) \, dm \\
\frac{I_x}{I_\beta} &= I_x^* \\
\frac{S_\beta}{I_\beta} &= \nu_\beta^2 \\
\frac{I_\theta}{I_\beta} &= I_f^*
\end{aligned}
$$

Approximation of I_x^* and I_f^* for a uniform blade

$$I_x^* = \frac{I_x}{I_\beta} = \frac{\int_e^R x_I \, (y-e) \, dm}{\int_e^R (y-e)^2 \, dm} = \frac{x_I \frac{(R-e)^2}{2} \rho_l}{\frac{(R-e)^3}{3} \rho_l} = \frac{3}{2} \frac{x_I}{R-e} \simeq \frac{3}{2} \frac{x_I}{R} \tag{1.1}$$

$$I_f^* = \frac{I_\theta}{I_\beta} = \frac{I_x + I_y}{\int_e^R (y-e)^2 \, dm} = \frac{\frac{m}{A} \left(\frac{ct^3}{12} + \frac{tc^3}{12} \right)}{\frac{(R-e)^3}{3} \rho_l} \simeq \frac{\frac{\rho R ct}{ct} \frac{tc^3}{12}}{\frac{R^3}{3} \rho ct} = \frac{1}{4} \left(\frac{c}{R} \right)^2 \tag{1.2}$$

Index

Bibliography

[1] M. M. Winston, "An Investigation of Extremely Flexible Lifting Rotors," Tech. Rep. NASA TN D-4465, Langley Research Center, National Aeronautics and Space Administration, Langley Station, VA, April 1968.

[2] M. M. Winston, "A Hovering Investigation of An Extremely Flexible Lifting Rotor," Tech. Rep. NASA TN D-4820, Langley Research Center, National Aeronautics and Space Administration, Langley Station, VA, October 1968.

[3] R. R. Pruyn and T. G. Swales, "Development of Rotor Blades with Extreme Chordwise and Spanwise Flexibility," *American Helicopter Society 20th Annual National Forum Proceedings, Washington D. C.*, pp. 102–108, 13-15 May 1964.

[4] Y. C. Fung, *An Introduction to the Theory of Aeroelasticity,*. John Wiley and Sons, Inc., New York, 1955.

[5] W. R. Davis, Jr., B. B. Kosicki, D. M. Boroson, and D. F. Kostishack, "Micro air vehicles for optical surveillance," *The Lincoln Laboratory Journal*, vol. 9, no. 2, pp. 197–214, 1996.

[6] M. McMichael, J., "Micro Air Vehicles - Toward a New Dimension in Flight," tech. rep., DARPA, July 1997.

[7] D. J. Pines and F. Bohorquez, "Challenges facing future micro-air vehicle development," *Journal of Aircraft*, vol. 43, pp. 290–305, April 2006.

[8] I. Chopra, "Hovering micro air vehicles: Challenges and opportunities," *Proceedings of International Forum on Rotorcraft Multidisciplinary Technology, Seoul, Korea*, October 2007.

[9] E. A. Fradenburgh, "The High Speed Challenge for Rotary Wing Aircraft," *SAE Paper #911974, Proceedings of the 29th International Pacific Air & Space Technolgy Conference, Nagoya City, Japan*, pp. 91–109, October 1991.

[10] W. Johnson, *Helicopter Theory,*. Dover Publications Inc., New York, NY, 1994.

[11] E. F. Katzenberger and E. S. Carter, *Vertical Flight: The Age of the Helicopter*, ch. The Technical Evolution of Sikorsky Helicopters, 1950-83, pp. 193–219. Washington D. C.: Smithsonian Institution Press, for the National Air and Space Museum, 1984.

[12] R. L. Goldman, "Some observations on the dynamic behavior of extremely flexible rotor blades," *IAS Paper No. 60-44, Presented at the 28th Annual Meeting of the IAS, New York, Jan. 25-27*, 1960.

[13] W. G. Roeseler, "The effect of ribbon rotor geometry on blade response and stability," Master's thesis, Massachusetts Institute of Technology, May 1966.

[14] B. Hein and I. Chopra, "Hover performance of a micro air vehicle: Rotor at low reynolds number," *Journal of the American Helicopter Society*, vol. 52, pp. 254–262, July 2007.

[15] J. Shen and I. Chopra, "Swashplateless Helicopter Rotor with Trailing-Edge Flaps," *Journal of Aircraft*, vol. 41, no. 2, pp. 208–214, 2004.

[16] I. H. Abbott and A. E. von Doenhoff, *Theory of Wing Sections,*. McGraw-Hill Book Company, Inc., New York, NY, 1949.

[17] E. J. Routh, *A Treatise on the Stability of a Given State of Motion, Particularly Steady Motion,*. Macmillan and co., London, 1877.

[18] I. M. Daniel and O. Ishai, *Engineering Mechanics of Composite Materials,*. Oxford University Press, 2006.

[19] S. J. Winckler, "Hygrothermally curvature stable laminates with tension-torsion coupling," *AHS/ARO International Conference on Rotorcraft Basic Research, Research Triangle Park, NC, February*, 1985.

[20] R. A. Ormiston, "Aeroelastic considerations for rotorcraft primary control with on-blade elevons," *American Helicopter Society 57th Annual Forum Proceedings, Washington, DC, 9-11 May*, 2001.

[21] H. Glauert, *The Elements of Aerofoil and Airscrew Theory,*. Cambridge University Press, and Macmillan Co, London, 1947.

[22] T. Theodorsen and I. E. Garrick, " Nonstationary Flow about a Wing-Aileron-Tab Combination Including Aerodynamic Balance," Tech. Rep. NACA-TR-736, Langley Research Center, National Advisory Committee for Aeronautics, 1942.

[23] A. Datta and I. Chopra, "Validation and understanding of uh-60a vibratory loads in steady level flight," *Journal of the American Helicopter Society*, vol. 49, pp. 271–286, July 2004.

Vita

Jérôme Sicard was born in Marseille, France on 29 July 1985, the son of Dr. Emile Sicard and Colette Sicard. He received the Bachelor of Science degree in Aerospace Engineering from the Institut Superieur de l'Aeronautique et de l'Espace (ISAE, Toulouse, France). He also studied for 2 semesters at the University of Wisconsin at Madison. Before starting Graduate School, Jerome Sicard worked one year at Altran as a structural engineer. There, he was involved in the mechanical dimensioning and environmental test validation of satellite antennas structures. Jerome's research interests include:

- Micro Aerial/Unmanned Vehicle design
- Rotorcraft design
- Spacecraft and satellite design

Permanent address: 54 avenue de Russie
03700 Bellerive sur Allier
France